Limitations of sector mesh geometry and initial conditions to model flow and mixture formation in direct-injection diesel engines

F. Perini[1], S. Busch[2], E. Kurtz[3], A. Warey[4], R.C. Peterson[4], R.D. Reitz[1]
[1]University of Wisconsin-Madison
[2]Sandia National Laboratories
[3]Ford Motor Company
[4]General Motors Company

Abstract

Sector mesh modeling is the dominant computational approach for combustion system design optimization. The aim of this work is to quantify the errors descending from the sector mesh approach through three geometric modeling approaches to an optical diesel engine. A full engine geometry mesh is created, including valves and intake and exhaust ports and runners, and a full-cycle flow simulation is performed until fired TDC. Next, an axisymmetric sector cylinder mesh is initialized with homogeneous bulk in-cylinder initial conditions initialized from the full-cycle simulation. Finally, a 360-degree azimuthal mesh of the cylinder is initialized with flow and thermodynamics fields at IVC mapped from the full engine geometry using a conservative interpolation approach. A study of the in-cylinder flow features until TDC showed that the geometric features on the cylinder head (valve tilt and protrusion into the combustion chamber, valve recesses) have a large impact on flow complexity. As a result, errors in near-TDC swirl ratio, vortex structure and turbulence availability were seen when employing sector meshing, even if a 360-degree sector, with direct IVC flow mapping, was used. During injection, lack of geometric details on the head led to the inability to predict the formation of an upper recirculation region on the tumbling plane, above the piston step, which has been associated with thermal efficiency benefits with the stepped-lip bowl. Initialization of the flow anisotropies in the cylinder resulting from the intake process at IVC were instead seen to have a smaller effect. The results also showed that tuning IVC quantities in a sector mesh cannot effectively compensate for its missing geometric and flow details.

Introduction

Comprehensive combustion calculations in realistic engine geometries need extensive computational resources, and predicted spray development can exhibit mesh dependency. Thus, in the engine design phase, a “sector” mesh approach is still currently employed, where one axisymmetric slice of the combustion chamber is modeled, under the assumption that both geometric and flow symmetries occur [1, 2, 3]. Sector meshing was established about thirty years ago, when coarse meshes were the norm due to limitations in available computing power, as an effective way to reduce the computational demand of engine simulations [4]. According to Amsden et al. [5], sector meshing could exploit n-fold symmetry in engine cylinders with multi-hole injectors, where an axisymmetric swirl-velocity field exists. Soon it was demonstrated that sector mesh simulations exhibited noticeable sensitivity on the initial (IVC) flow conditions, for example when mapping the initial conditions from different sectors of a full-mesh simulation [6]. Despite that shortcoming, the sector approach proved extremely successful at diesel engine parametric studies and optimization of combustion strategy and chamber design (see [7, 8, 9, 10] for a few examples).

As diesel engine design and operation develops towards more complex piston geometries, such as chamfered- or stepped-lip bowls [11] and low temperature combustion strategies, correct prediction of in-cylinder flow phenomena becomes more relevant as tighter trade-offs between operating parameters are needed [12]. This is highlighted in Figure 1, where a conventional diesel combustion mode is simulated employing either a full-cycle, full mesh model, or a sector mesh one, in an engine equipped with a stepped-lip bowl. Combustion evolution fundamentally differs between the two approaches: a sector mesh exhibits earlier ignition, earlier CA50, as well as lower average heat release rate than for the full mesh simulation, despite IVC initialization from full mesh data for both cases. This discrepancy also has implications on how spray models, as well as combustion kinetics models, are validated against internal combustion engine cases.

In order to quantify the errors descending from the sector mesh approach in advanced combustion simulations in direct-injection diesel engines, we studied CFD simulation behavior by modeling the Sandia small-bore optical diesel engine facility. A well-validated, full-geometry model of the engine, built with the FRESCO CFD platform [13], was used as the reference case. A single operating condition, representing a medium-load, slightly boosted operating point, with two pilot-main injection strategies, was considered. Three modeling approaches were compared:

- Full engine geometry with body-fitted mesh for high accuracy, including valves and intake and exhaust ports and runners. Full-cycle flow simulation before fired TDC;
- Axisymmetric sector mesh ($1/7^{th}$ of the combustion chamber). IVC-to-EVO simulation initialized with homogeneous bulk in-cylinder conditions;
- 360-degree azimuthal mesh of the cylinder (360-degree sector structure). IVC-to-EVO simulation initialized with mapped fields from the full engine case.

The paper is structured as follows: first, the computational setup is described. Second, the meshing approaches, their approximations, and field initialization are discussed. Then, the results from simulations of a conventional diesel combustion case with a pilot-main injection strategy are discussed: flow and turbulence features, as well as their effects on predicted mixture formation. Analysis of the results provides a better understanding of the causes for discrepancies in the predicted in-cylinder mixture formation with the sector mesh approach, highlighting the dominant role of seemingly subtle geometric details over flow field initialization.

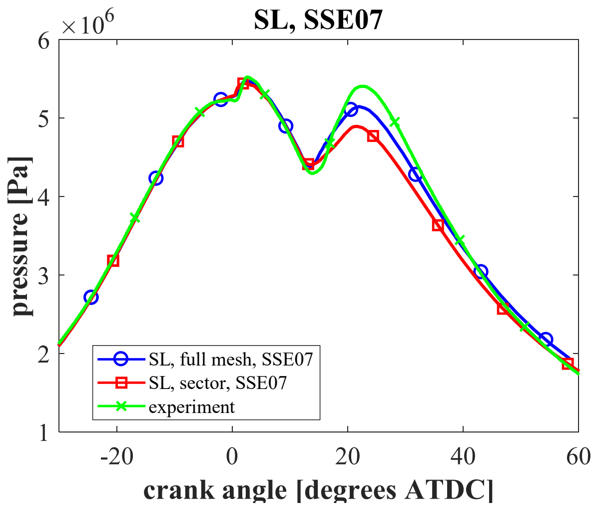

Figure 1. Predicted and experimental in-cylinder pressure traces for a combusting simulation: CDC9, injection strategy: SSE=-07.

Simulation setup

The FRESCO CFD simulation platform was employed to model the engine. The code implements an unstructured, parallel volume-of-fluid solver for the Navier Stokes equations with automatic domain decomposition for variable-topology meshes. More details about FRESCO are given in [13]. Turbulence is modeled using a generalized re-normalization group (RNG) turbulence closure model that has been validated with engine flows, as well as for impinging and reacting jets [15]. Fuel injection and spray phenomena are modeled with a Lagrangian-Droplet/Eulerian-Fluid (LDEF) approach. Table 1 is a summary of the sub-models used to simulate turbulence and sprays.

Table 1. Computational model setup employed for the current study.

Phenomenon	**Sub-model**
Turbulence	Generalized re-normalization group (GRNG) k-ε [14, 15]
Injection	Blob model with dynamic blob allocation [16]
Spray angle	Reitz and Bracco [17]
Spray breakup	Hybrid KH-RT instability, Beale and Reitz [18]
Near-nozzle flow	Unsteady gas-jet model with implicit momentum coupling [16]
Drop drag	Analytical with Mach number effects [16]
Droplet collision	Deterministic impact; bounce, coalescence, reflexive separation, and stretching separation [19]; dynamic radius of influence [16]
Evaporation	1D discrete multi-component fuel [20]
Piston compressibility	Static, Perini et al. [21]

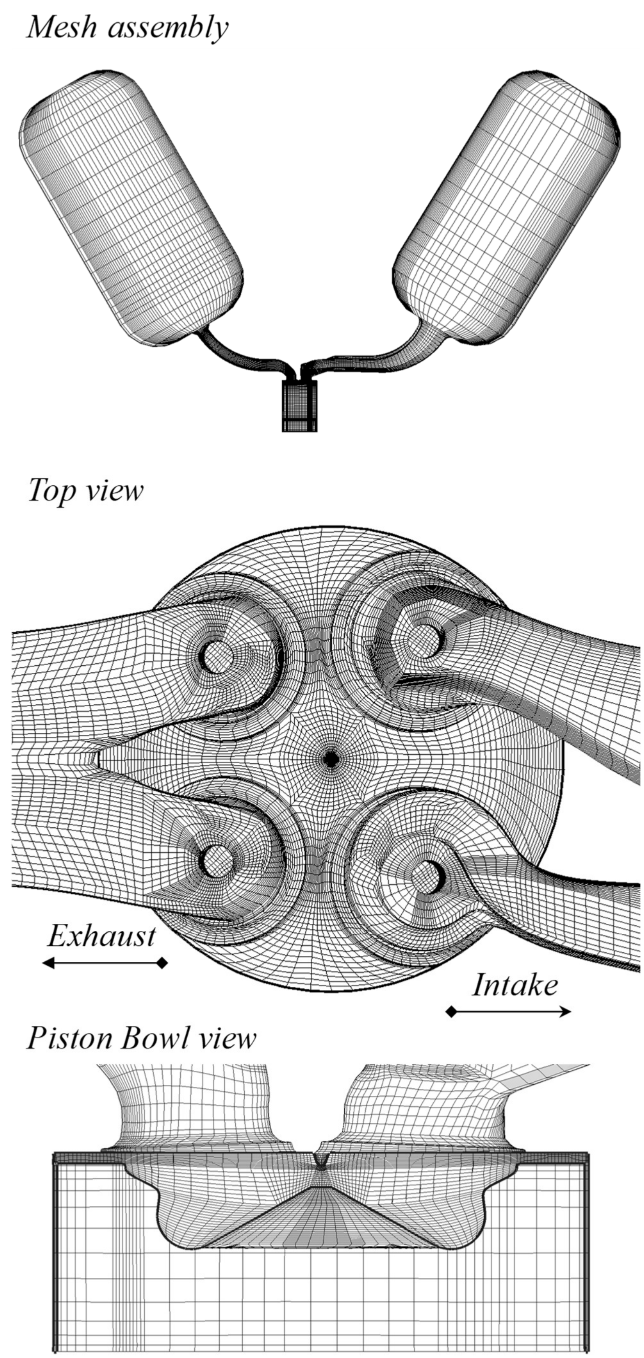

Figure 2. Full-engine CFD mesh used in this study. Cutaway views are shown to depict each piston bowl. The large intake and exhaust plenums are accurate representations of the single-cylinder research engine setup.

The spray sub-model parameters have been simultaneously optimized with a multi-objective genetic algorithm based on Engine Combustion Network (ECN) spray A data [22]. No further tuning was performed for the current study, as comparisons with experimental liquid and fuel vapor data showed very good agreement (see, for example, [23]).

The Sandia small-bore optical diesel engine platform, was used in this study. The full engine geometry included the intake and exhaust surge tanks in the optical facility; intake and exhaust runners, which embed swirl plates for variable swirl ratio operation; as well as the intake and exhaust ports, cylinder, and the optical piston. The piston features a stepped-lip bowl design, which has been shown to enable significant efficiency and soot emission gains over conventional, re-entrant bowl designs for late injection timings (See [24, 25]).

Table 2: Engine and fuel injector geometry data

Bore	82.0 mm
Stroke	90.4 mm
Connecting rod length	166.7 mm
Squish height	1.36 mm
Geometric compression ratio	15.8 : 1
Injector nozzle holes x diameter	7 x 139 µm
Nozzle hole conicity (k_s)	1.5
Injector opening angle	149°

Table 3: Engine operating point and simulation boundary conditions. Note the naming convention for the three injection timings.

Engine speed	1500 rpm		
Intake pressure	151 kPa		
Intake temperature	329 K		
Coolant temperature	363 K		
Piston surface	440 K		
Liner temperature	430 K		
Head temperature	440 K		
Intake valve	370 K		
Exhaust valve	400 K		
Intake port	329 K		
Exhaust port	410 K		
Exhaust pressure	145.7 kPa		
Intake charge	100 vol% N_2 (non-combusting)		
Swirl ratio (Ricardo)	2.2 (both intake swirl plates open)		
Fuel	58 vol% 2,2,4,4,6,8,8-heptamethylnonane, 42 vol% n-hexadecane		
Injection pressure (baseline)	800 bar		
Pilot-main hydraulic dwell	11.5 CAD		
Injection timing		Near-TDC (SSE17)	Intermediate (SSE07)
	Pilot SSE (CAd bTDC)	17.0	7.0
	Main SOI (CAd bTDC)	0.9	-9.1

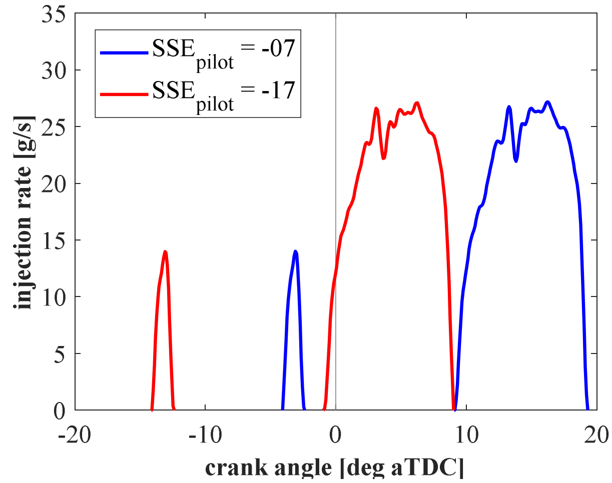

Figure 3. Simulated injection rate profiles for the two injection strategies [26].

Engine geometric data is summarized in Table 2, as available on the ECN website [27]. An unstructured, body-fitted, hexahedral mesh is generated for the full engine model [28], and contains approximately 724,000 cells at bottom dead center. The mesh is depicted in Figure 2. Details of the 7-hole injector used in this study are also given in Table 2. Spray targeting in the simulation matches the spray targeting used in corresponding optical and thermodynamic engine experiments and has been adjusted for each piston. The specific spray targeting data used in this study are available on the ECN website, as well as measured injection rate data for the baseline cases [26].

Consecutive cycles are simulated to reach acceptable convergence of the flow field prediction at IVC, while keeping the total computational time reasonable, as follows. The simulation is initialized at the time of exhaust valve opening of cycle 0. The in-cylinder flow field is initialized as solid body rotation with a small residual swirl level (Rs = 0.05). Turbulence levels, density, pressure, temperature, and composition are initialized as homogenous for each of three regions: (1) cylinder; (2) intake ports, runners, and surge tank; (3) the exhaust ports, runners, and surge tank. Cycle 1 is simulated in its entirety but without fuel injection. Results of previous investigations indicate that after this cycle, the most significant features of in-cylinder flow are well converged [29]. Fuel injection takes place during cycle 2, where all results shown in this work are taken.

Engine operating conditions for simulation setup are given in Table 3 and represent corresponding experimental conditions for which experimental data are available [30]. The engine operating point represents a part-load (9bar IMEP), conventional diesel combustion strategy (CDC9) with a split pilot-main injection strategy. Injection takes place in a non-reacting environment with 100% N_2, as the experimental results have been evaluated using fuel tracer planar laser-induced fluorescence (PLIF) images. Two injection schedules were employed, where the pilot-main dwell is held constant, and the whole injection rate law is block shifted. They are identified by start of solenoid energizing (SSE) timing for the pilot injection: a SSE=-17 deg aTDC, or "near-

TDC" main injection, has a main injection pulse being injected shortly before top dead center; SSE=-7 deg aTDC, or "intermediate" injection timing, leads to efficiency and emissions advantages over the conventional piston when fired, and the main injection pulse starts at approximately 9.1 CA deg aTDC [24].

Baseline injection rate profiles are measured with a hydraulic injection rate meter based on the injector solenoid energizing times used in engine testing for each main injection timing, and are represented in Figure 3. For details of the experimental setup used to measure injection rates, see [26].

Meshing approaches

Three meshing strategies were compared: a full-mesh, full-flow field initialization approach; an axisymmetric sector-mesh approach which represents only one injector nozzle or 1/7th of the combustion chamber; a 360-degree sector-mesh approach that represents the whole closed-valve combustion chamber in the same way as the axisymmetric sector, but does not require a flow axisymmetry constraint. The three meshes employed in this study are represented in Figure 4.

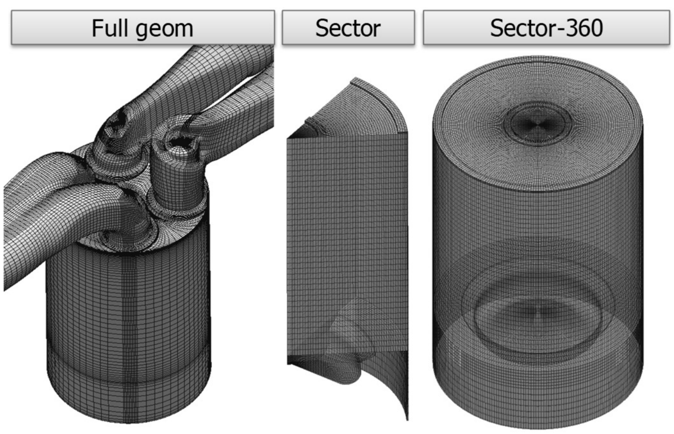

Figure 4. Mesh structure comparison. Left: full engine geometry; Center: Sector geometry (1/7th sector of the cylinder); Right: Sector-360 geometry.

Full mesh. This model represents the most accurate representation of the optical engine geometry, providing accurate flow field representation at IVC thanks to a full-cycle simulation of the charge exhaust and intake [29]. The body-fitted computational mesh, as represented in Figure 2, was built with focus on appropriate near-wall boundary layer modeling at the liner and in the bowl, for capturing large-scale in-cylinder swirl, as well as surrounding each valve, to appropriately capture smaller-scale helical flows forming during the intake stroke. During the closed-valve part of the engine cycle, all geometrical details of the cylinder head are preserved. These include the valve recesses in the head, the injector tip protrusion, as well as non-vertical, canted (by a 2 degree tilt) intake and exhaust valves that protrude slightly into the combustion chamber. An average cell size of 0.7 mm was employed, with peak cell count of 724k cells at BDC. The average cell size was selected based on a previous grid convergence study on the same engine [31]. A comprehensive review of the full engine mesh modeling approach employed in this study can be found in [28, 29].

Sector. The sector mesh models an azimuthal sector of one seventh of the combustion chamber, corresponding to the azimuthal semi-region surrounding one injector nozzle axis. The mesh is delimited by two vertical-plane periodic boundary conditions which impose axial symmetry to all simulated fields. In order to accurately model the geometry, the mesh was built starting from the full-mesh simulation snapshot at IVC. First, both head and top piston surface vertical locations were enforced to be same at IVC as with the full mesh. This guarantees that the same relative injector-piston targeting is achieved. The actual valve recesses cannot be represented in a sector mesh since they are not axisymmetric. However, their footprints were modeled as as annular segments cut into the head surface, having the same average radial locations and width as the actual valve recesses (approximately 2 mm). This makes up for a same-volume, axisymmetric equivalent of these structures. Finally, the mesh was discretized such that the same average cell resolution as in the full engine mesh was obtained.

Flow field initialization in the sector was made following simulation data at IVC from the full mesh simulation. In general, it would be possible to apply direct mapping of all fields. However, the sector symmetry would quickly take the flow field and its initial non-uniformities back to a symmetric swirling flow, making tumbling components useless (see [31]), and quickly dissipating initial turbulence [28]. Furthermore, sector meshes are usually employed for large parametric studies where with inputs as global parameters. Hence, we employed the following strategy:

- IVC thermodynamics (pressure, temperature, composition) and turbulence (TKE, length scale) fields are initialized as homogeneous, from the cylinder averages in the full mesh simulation.
- The swirling flow field is initialized with a bulk swirl ratio and tangential velocity profile that are inferred from the full mesh flow field at IVC, as follows.

<u>Swirl ratio initialization</u>. Bulk swirl ratio initialization is based on angular momentum conservation. The radial profile of tangential velocities is an additional parameter that describes the radial density of angular momentum. It was observed to depend on the intake port configuration and instantaneous swirl ratio [32]; it is therefore important to accurately model the radial profile of tangential velocities to reliably approximate the flow fieldy despite axisymmetry. To this end, the following Bessel function formulation is used to model tangential velocity [5]:

$$u_\theta(r) = \frac{\omega\, R_s \alpha}{4\, B_{j,2}(\alpha)} B_{j,1}\left(\alpha \frac{r}{R}\right) \tag{1}$$

a tangential velocity profile versus radius (r) depends on a unique parameter α, given cylinder radius R, engine speed ω and bulk swirl ratio R_s. The differential formulation using Bessel functions $B_{j,1}$ and $B_{j,2}$ is such that the total angular momentum does not depend on α. As reported in Figure 5 for a sample case, $\alpha \in [0, 3.83]$, where $\alpha = 0$ represents solid body rotation, while higher values of α lead to higher velocities in the central region and lower velocities close to the liner, until a no-slip condition at the liner is encountered for $\alpha_{max} = 3.83$.

In our sector approach, α at IVC was inferred from the full mesh flow field, as represented in Figure 6. In-cylinder tangential velocities are binned in 100 radial bins, and an azimuthal average is computed for each bin; then, a least-squares fit against the bin-averaged tangential velocities is then computed to find α Figure 6 also shows the standard deviation of the binned velocities in the azimuthal set at each radial location. The flow initialization in the sector approach applies the same tangential velocity profile from the two coefficients (*Rs,* α) to all axial locations in the cylinder [5].

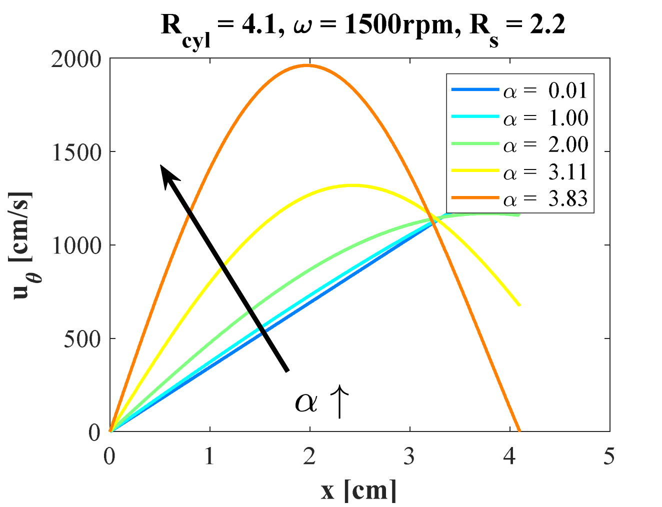

Figure 5. Radial profile of tangential velocity according to the formulation of [5], for the current engine (R = 4.1 cm, ω = 1500 rpm, Rs = 2.2).

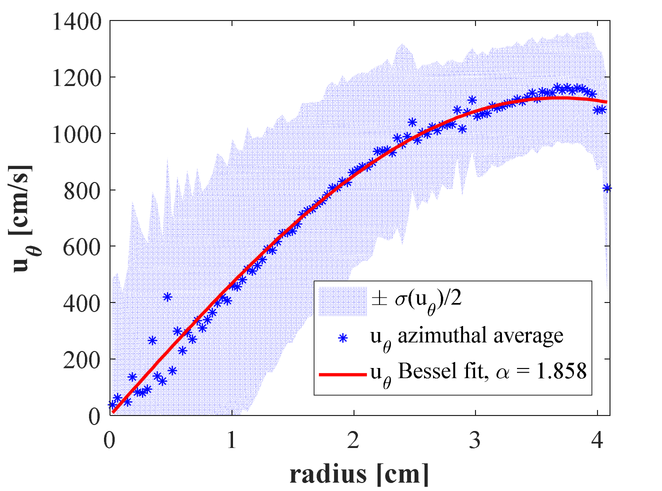

Figure 6. Tangential velocity profile reconstruction from fhe full mesh flow field at IVC. Blue marks: bin-averaged tangential velocities from the CFD simulation. Red: reconstructed tangential velocity profile.

Sector360. A full-circle, 360-degree sector mesh approach was established to separate the effects of meshing from those of symmetry and simplified initialization. The sector-360 mesh has the exact same discretization as the sector mesh, both azimuthally and on the vertical plane; but, it is azimuthally extended through the whole 360 degrees, as shown in Figure 4. Similarly to the sector case, the mesh is spray-oriented and axisymmetric, so the same mesh structure will be experienced by all 7 spray jets. The central region close to the cylinder axis was replaced with a structured rectangular block, to remove *axis* cells which would degenerate into triangular prisms, thus leading to excessively small time-step constraints due to the CFL number condition, and potentially biasing the simulation results towards greater axisymmetry (no fluxes can cross a degenerate face according to the advection algorithm).

Also, no changes were made to the head geometry configuration: the sector-360 mesh retains the same horizontal-valve-surface and annular-symmetric recess representation as the sector mesh.

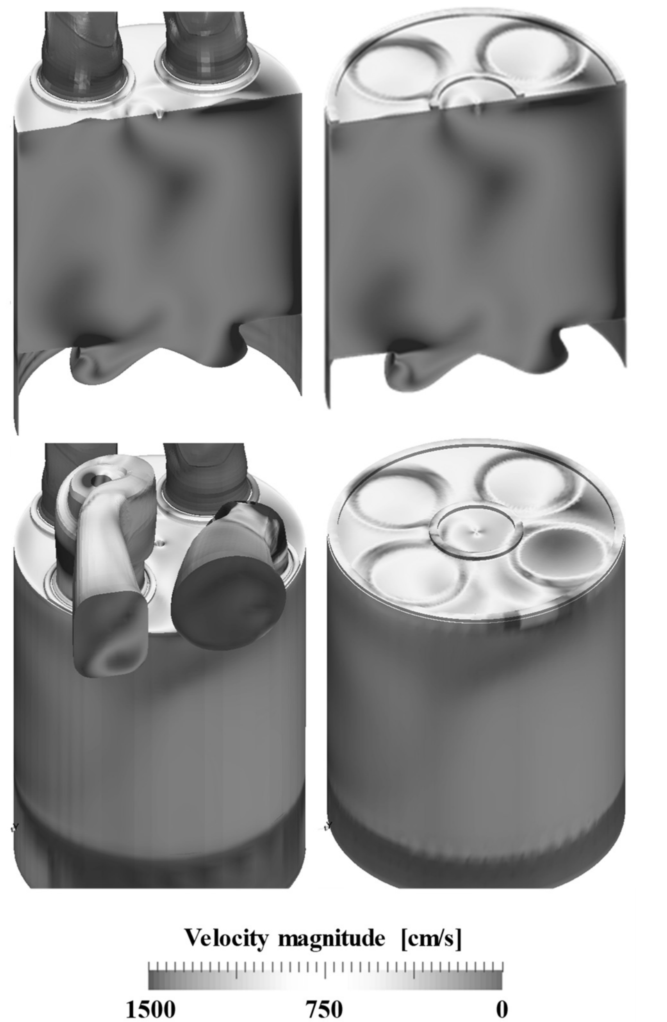

Figure 7. Velocity field mapping at IVC (588 deg aTDC). Left: full mesh with actual simulation results; right: sector-360 mesh with mapped field data

<u>Mapped field initialization</u>. Since the sector-360 mesh has no periodic boundary conditions, it is possible to initialize all fields as directly mapped from the full mesh at IVC. To this end, a conservative field mapping procedure was developed and implemented to provide the most accurate initial conditions to

the sector-360 mesh. Details on the mapping scheme are reported in the Appendix; an example of flow field mapping at IVC is represented in Figure 7, where velocity magnitudes are compared. The sector-360 simulation hence only differs from the sector simulation in that it employs a non-symmetric, non-homogeneous field solution, onto the same simplified geometric representation. Finally, Table 4 summarizes a comparison of the modeled features using each meshing approach.

Results and discussion

In-cylinder swirling flow

Because the local swirl ratio in the near-TDC range is crucial to mixture formation in conventional diesel combustion, its development was studied first. In-cylinder swirl ratio histories, according to the full-mesh mixture formation simulation, could not be captured by using the sector mesh approach, as reported in Figure 8.

Table 4: Summary of geometry modeling approaches.

Feature	Full	Sector	Sector-360
Simulated cycle	Full Exhaust + Intake strokes + IVC to EVO	IVC to EVO	IVC to EVO
Meshing	Body-fitted	Axisymmetric	Axisymmetric with central O-grid
Head geometry	Exact Valve recesses, protrusion, canted (+2 deg)	Axisymmetrized: horizontal head, annular recesses (h ~ 2.1 mm). Exact recess volume and radial location	
IVC flow field	From full-cycle initialization	Synthetic (Rs, α)	Mapped from full mesh
IVC turbulence	From full-cycle initialization	Homogeneous	Mapped from full mesh
IVC composition	From full-cycle initialization	Homogeneous	Mapped from full mesh
IVC thermo properties	From full-cycle initialization	Homogeneous	Mapped from full mesh

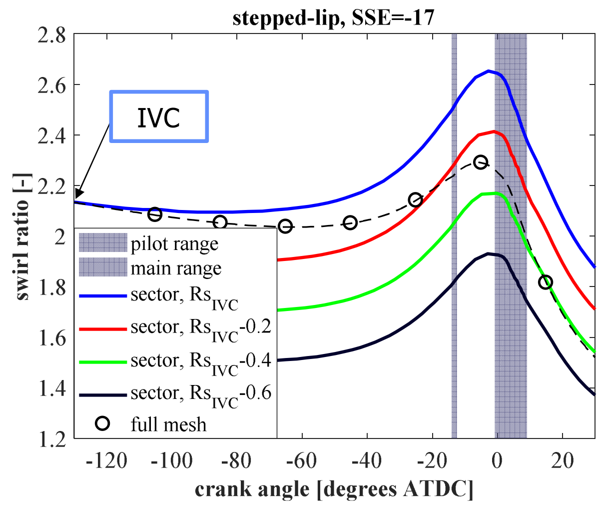

Figure 8. Predicted in-cylinder swirl ratio histories with a sector mesh, compared with the full mesh simulation. $R_{s,IVC}$ obtained from predicted flow field in the full mesh case.

The full mesh simulation predicted an initial decay in swirl ratio during the late intake and early compression strokes, likely as a result of the strong flow non-uniformities still present at IVC due to the large vertical velocities from the intake mixing with already-formed bore-scale (from the tangential port) and small-scale (from the helical port) vortices [29]; and due to the dissipative nature of the liner wall boundary. As the piston got close to TDC, the swirl ratio increased thanks to the smaller inertia of the piston bowl contents, but also fostered by the squish mechanism, where fluid with large tangential velocities is driven radially inward.

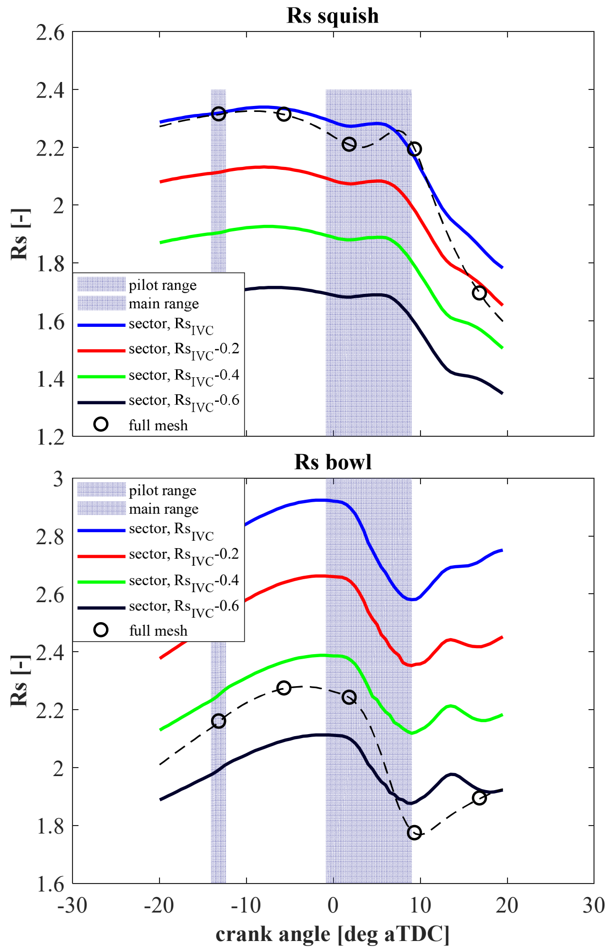

Figure 9. Full vs. sector mesh swirl ratio comparison: (top) squish volume; (bottom): piston bowl volume.

According to the symmetry-driven sector mesh, minimal swirl decay is seen without flow uniformities, as well as a faster rate of increase close to TDC. This led to a higher near-TDC swirl-ratios with the sector mesh. After TDC, when most swirl non-uniformities were destroyed by the tiny squish height [33], and by the stabilizing effect of the injection, a similar swirl ratio decay as for the full mesh was seen.

The IVC swirl ratio was tuned in the sector mesh until a similar near-TDC swirl ratios could be achieved, whereby a swirl ratio reduction of 0.4, or approximately 18%, was needed. However, it was impossible to match the swirl ratio history during both the pilot and main injection events, or throughout the compression stroke. This may cause even more inaccurate spray penetration predictions in advanced combustion modes that feature early injections. Also, conservation of angular momentum while computing the advection terms in FRESCO was enforced when employing the sector mesh. Its deactivation did not yield noticeable differences in swirl ratio trace.

Further insight into the swirl ratio evolution in the sector mesh is provided by region-based swirl ratio computation between the squish and bowl regions, according to the procedure outlined in [33] andreported in Figure 9. Swirl ratio in the squish region was best captured with the same IVC R_s value as with the full geometry, while swirl ratio in the piston bowl was matched only when the IVC value was reduced by -0.6.

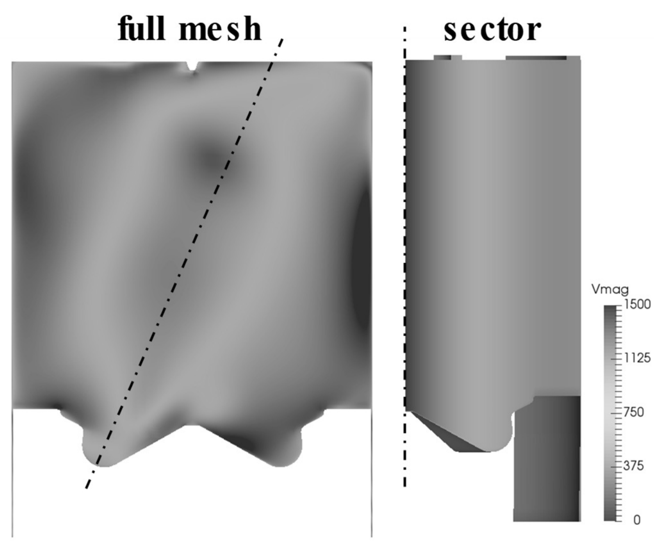

Figure 10. IVC velocity magnitude field comparison between full mesh and sector mesh approaches. Dashed lines: pictorial view of the swirl vortex axis.

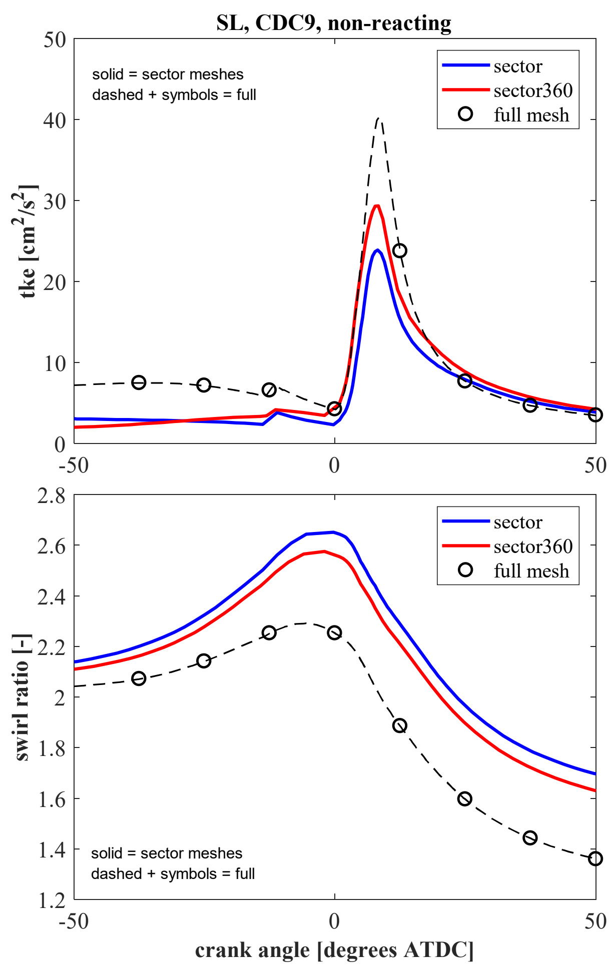

Figure 11. Predicted in-cylinder turbulence kinetic energy (top) and

swirl ratio (bottom) with three mesh approaches: full mesh (black with marks), sector (blue), sector-360 (red).

Velocity magnitude fields in Figure 10 suggest that the cause for that discrepancy is the tilt and wobbling of the swirl vortex: the swirl vortex axis in the full-cycle simulation enters the bowl with strong eccentricity. Because the swirl center is so eccentric, swirl ratio in the bowl is low; the swirl center than keeps rotating (precessive motion) throughout the compression stroke, maintaining bowl swirl ratio low.

Swirling flow and head geometry

Despite enjoying a more realistic non-axisymmetric flow field initialization, also the sector-360 approach yielded much larger in-cylinder swirl ratios than predicted by the full mesh, as was observed with the sector geometry. This phenomenon is represented in Figure 11, together with corresponding bulk in-cylinder turbulence kinetic energy histories.

Much lower in-cylinder turbulence during the whole compression stroke was common to both sector mesh approaches in comparison with the full mesh, and added up to -62% for the sector mesh. The same phenomenon also held during early injection, even if to a lesser extent, up to -21% for the sector-360 case.

The inability of the sector-360 case to generate nearly as much turbulence as the full mesh showed that initial turbulence level and flow field non-uniformity does not significantly affect turbulence generation in the engine, Thus, strain rates [15] from the initially non-well-formed swirl vortex are not the primary source of turbulence kinetic energy. Instead, geometric details of the cylinder head appear to play an important role, as represented in Figure 12.

Looking at an in-cylinder velocity magnitude field close to the firedeck from above the head at 50 degrees before TDC, significant differences between the three modeling approaches are visible. The sector mesh still produces a Bessel-shaped swirling velocity profile as it had since IVC, as the intensity of the squish flux is still low, and there are no non-symmetric geometric details that could introduce changes in that flow structure. The sector-360 geometry has a much different flow footprint than the sector mesh, but in presence of greater velocity magnitude variance, the sector meshes both produce similar bulk swirl ratios. The flow field in the sector-360 model exhibits instantaneously higher velocities at the left-hand-side (exhaust). In the sector-360, non-uniformities from IVC initialization still survive, and are located at somewhat similar azimuthal locations as those being predicted by the full geometry. However, the velocity field is much smoother azimuthally, as all geometry details are axisymmetric.

Instead, in the full engine geometry, four neat flow separation regions are present at each leading edge formed by the valve recesses with the cylinder head. Non-azimuthal valve recesses and slightly canted valves represent the only geometric differences between the full and sector-360 meshes. These separation regions are responsible for disrupting the azimuthal flow and introducing additional turbulence and small-scale recirculation regions, thus decreasing azimuthal velocities and therewith the swirl ratio.

<u>PIV comparison.</u> A comparison between predicted and measured in-cylinder velocities using particle image velocimetry [29] confirms these discrepancies close to the firedeck and through the end of the compression stroke. In Figure 13, tangential velocity profiles with all mesh approaches are shown for a horizontal cut-plane located 3mm

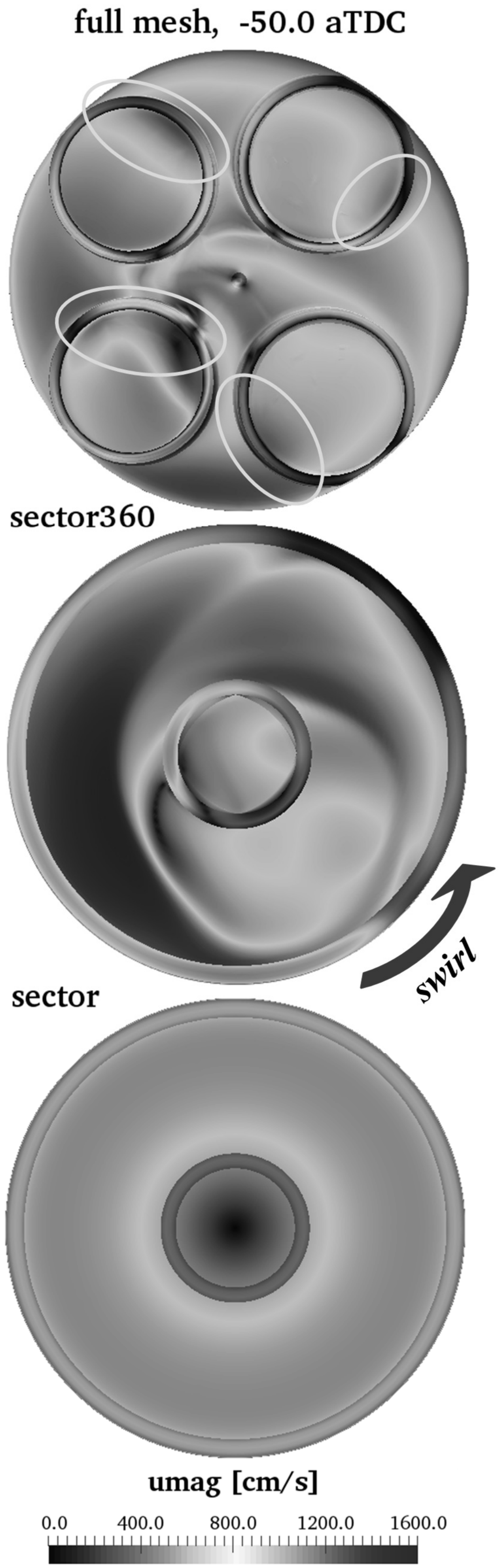

Figure 12: Velocity magnitude contours during the compression stroke (at 50 deg bTDC) as seen from above the cylinder head, for three mesh approaches: full mesh (top), sector-360 (center), sector (bottom). Flow separation regions highlighted with gray circles.

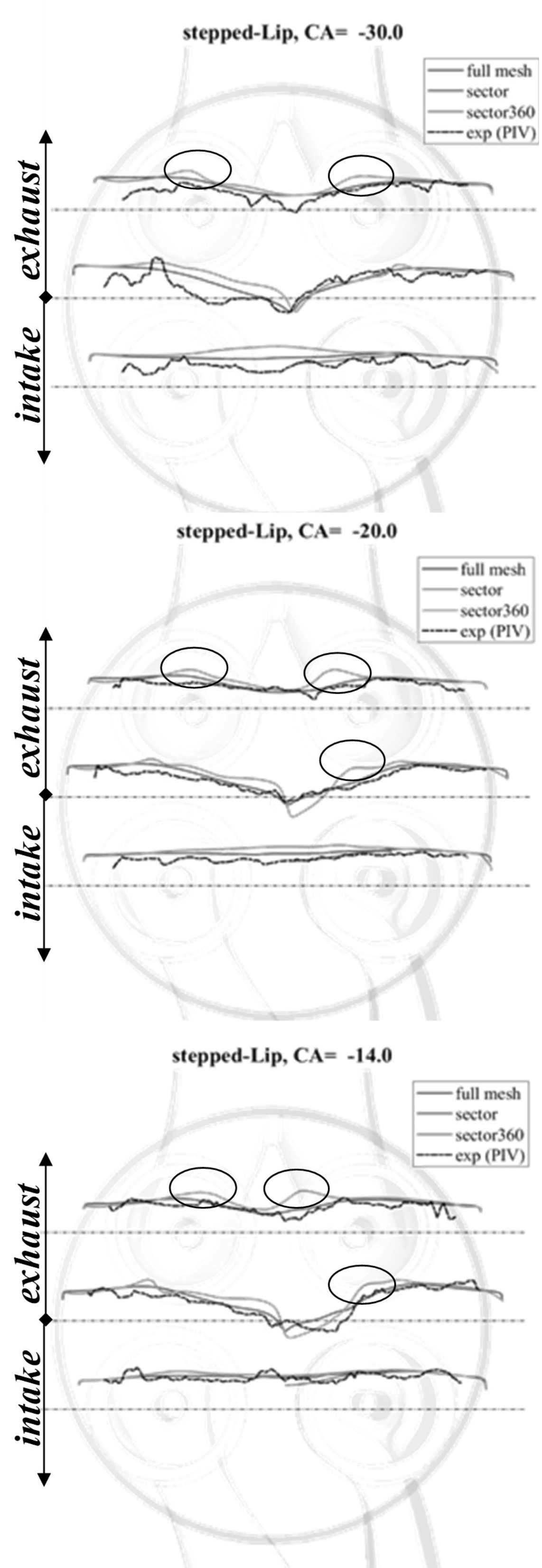

Figure 13. Predicted vs. experimental (PIV) tangential velocity profiles at a horizontal plane located 3mm from the firedeck during the compression stroke [34].

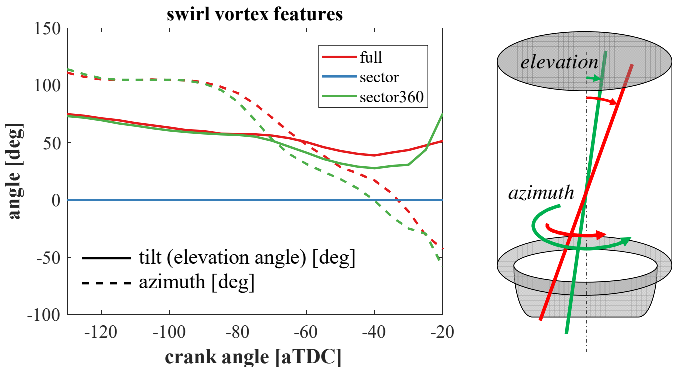

Figure 14. Predicted swirl vortex elevation (tilt) and azimuthal angles during the compression stroke: meshing approach comparison.

below the fire deck. The full mesh approach provided the best local swirl ratio and swirl center predictions at all three crank angles tested. The sector-360 mesh predicted excessively large tangential velocities instead. These larger tangential velocity profiles exhibit spikes that are located close to the radial location of the axisymmetric "compensatory" annular recess.

Vortex structure. In order to quantify whether the geometric differences at the head could lead to noticeable differences in the bulk swirl vortex structure, the swirl vortex's tilt and precessive movement were analyzed using the Principal Component Analysis (PCA) model reduction procedure as outlined in [33]. The results are reported in Figure 14: the full-mesh vortex is *more tilted*, and with slower precession velocity - the vortex axis's azimuthal angle decays slower than what the sector-360 predicts.

To understand whether the vortex structure discrepancy was generated by the flow separation regions created by head geometry details, the vertical distributions of in-cylinder swirl ratio and in-cylinder tangential velocity profile parameter α were analyzed. As Figure 15 shows, close to top dead center, the swirl ratio in the bowl is larger for the sector360 case, with a comparable tangential velocity profile; this is consistent with the swirl vortex being less tilted such that the swirl axis is more centered in the bowl, leading to a higher swirl ratio, as observed in Figure 9. In the squish region, instead, the bulk swirl ratio is similar between the two mesh approaches. However, larger α is observed with the sector-360 mesh: without non-azimuthal geometry details, larger tangential velocities exist in the central region of the cylinder as they are not modified by the complex interaction at the non-azimuthal valve recesses. It was also observed that the squish mechanism has identical behavior between the sector and full mesh approaches, so, it cannot be responsible for the generation of larger velocities as the piston surface gets closer to the head.

Mesh resolution. Finally, in order to rule out a potential role of the azimuthal mesh resolution on the swirl prediction between the sector-360 and the full mesh, two additional revisions of the sector-360 mesh were made by coarsening the number of azimuthal cell layers: the reference mesh as the "refined" one, a "medium" mesh with 60% azimuthal layers, and a "coarse" mesh with 20% azimuthal layers. Both these meshes had the same exact discretization on the vertical plane as the refined ones. A comparison in predicted swirl ratios, as well as azimuthal mesh structure footprints, is reported in Figure 16. Only slight differences in swirl ratio could be observed when the coarse mesh was used, while no differences were observed when using the medium mesh. The extent to which swirl ratio with the coarse sector-360 mesh differs from the

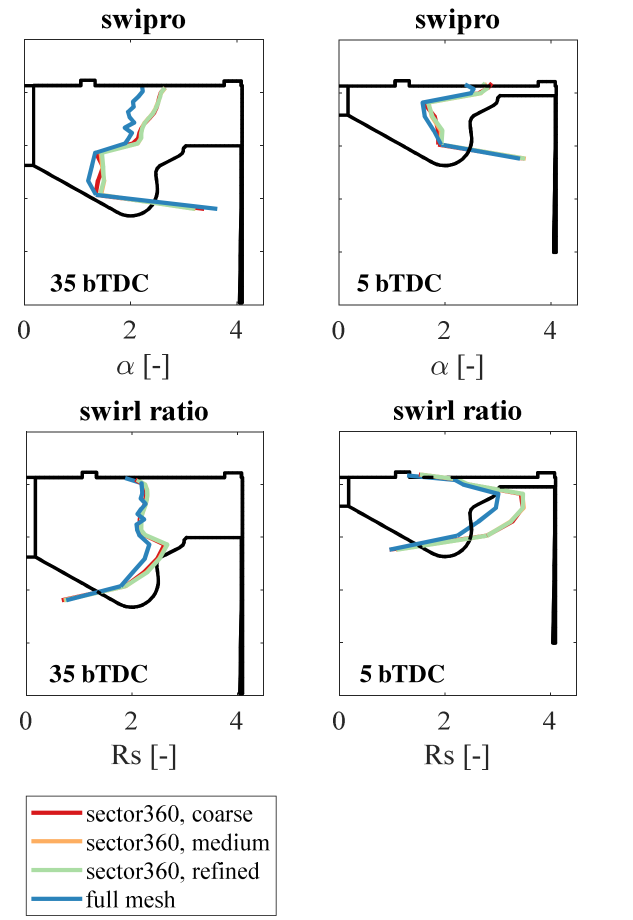

Figure 15. Vertical distribution of radial tangential velocity parameter α (top) and swirl ratio (bottom) during compression, close to TDC. Meshing approach comparison.

refined sector-360 is not comparable with the discrepancy with sector-260 and full mesh approaches, so azimuthal resolution can not be identified as responsible for these large-scale differences.

Heat transfer

Heat transfer through the walls was analyzed as local near-TDC temperatures could affect a mixture's ability to ignite, especially as it falls in the negative temperature-coefficient (NTC) range for typical hydrocarbon fuels, such as DPRF58, when running the current CDC9 operating condition (see [35] for ignition delay behavior of the DPRF surrogate).

Predicted wall heat transfer rates, as well as bulk in-cylinder temperatures are reported in Figure17. Despite the higher bulk swirl ratio throughout the compression stroke, both sector approaches predict lower wall heat transfer than the full engine mesh. The reduction was seen to be up to -9% in heat transfer rate, which led to higher in-cylinder temperature of up to +11K at top dead center versus the full mesh prediction. Both these behaviors are explained by the different predicted swirl vortex structures: in the sector simulations, the largest tangential velocity components are located in the central part of the cylinder (α↑), while the full mesh predicts larger tangential velocities closer to the wall (α↓), which generate greater viscous stresses and higher turbulence. According to the wall heat transfer function of [36]:

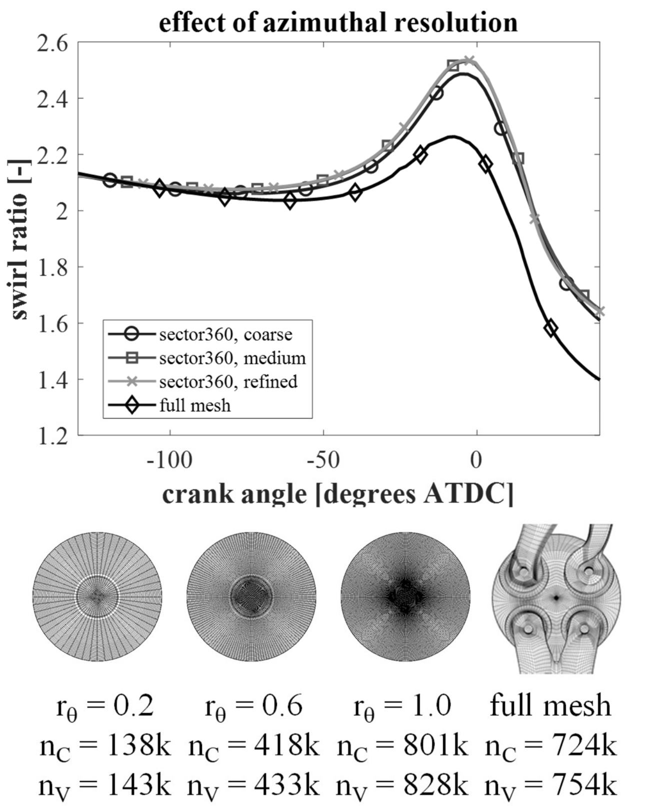

Figure 16. Azimuthal resolution effects on predicted in-cylinder swirl ratio with a Sector-360 mesh approach. Azimuthal resolution factors: rθ = 20% (coarse), 60% (medium), 100% (refined).

$$q_{wall} = \frac{\rho c_p u^* T \ln(T/T_{wall})}{2.1\ln(y^+)+2.5}; \qquad (2)$$

where ρ is the ambient density, c_p constant-pressure specific heat, T the cell's temperature, T_{wall} the wall face temperature and y+ the nondimensional boundary coordinate; this formulation leads to higher wall heat transfer proportional to the increase in dimensionless velocity, $u^* = c_\mu^{0.25}\sqrt{k}$. Hence, the cumulative heat loss during the compression stroke was dominated by the local swirl flow structure at the walls rather than by bulk swirl ratio.

During the injection a larger heat loss due to the impinging jet against the piston surface was seen in both sector cases. This phenomenon is dominated by the bulk swirl ratio, as the impingement occurs at the step location r ~ 2.1 cm, or approximately half the cylinder bore. Here, the jets are subject to larger azimuthal spreading due to the higher swirl ratio and larger tangential velocities (α↑). This increases the size of high-momentum impingement areas and leads to higher rates of wall heat transfer on the piston surface compared to the full mesh prediction.

Mixture formation

The ability to form an upper recirculation region in the tumbling plane, which is responsible for better air utilization in the upper cylinder region close to the squish, is associated with faster mixing and higher thermal efficiency in diesel engines equipped with stepped-lip bowls when compared to conventional re-entrant bowls

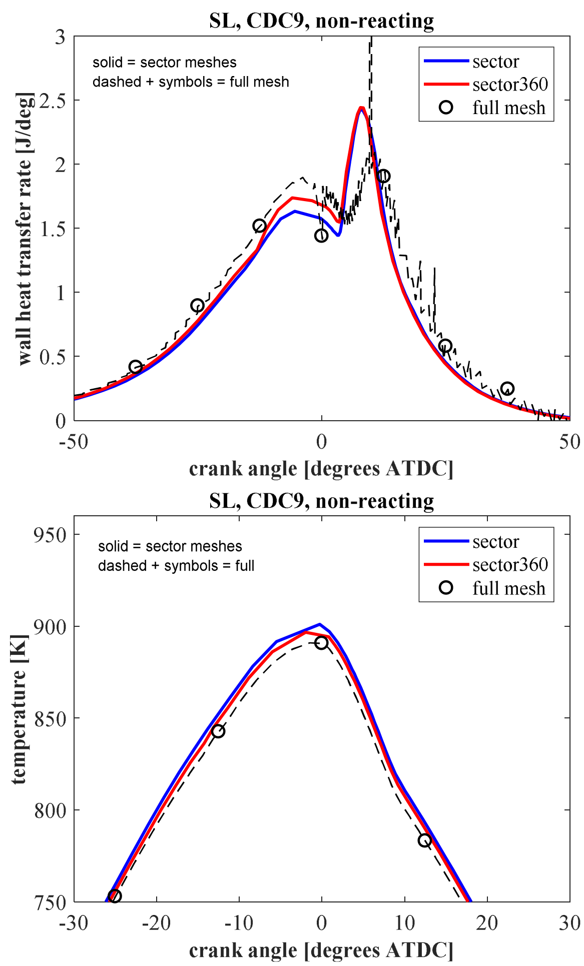

Figure 17. Predicted wall heat transfer rate (top) and bulk in-cylinder temperature (bottom): meshing approach comparison.

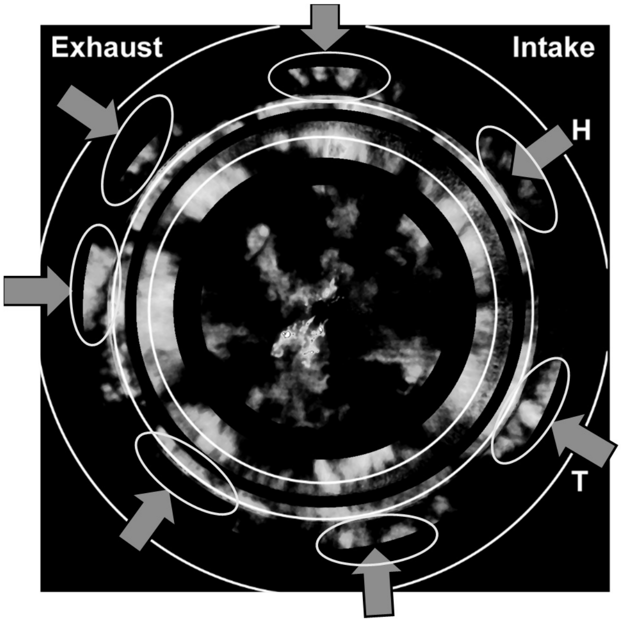

Figure 18. Fuel tracer PLIF at 12 deg aSOI for a partially-premixed injection strategy in the stepped-lip piston geometry. Regions of fuel encroachment from the outer regions highlighted with arrows.

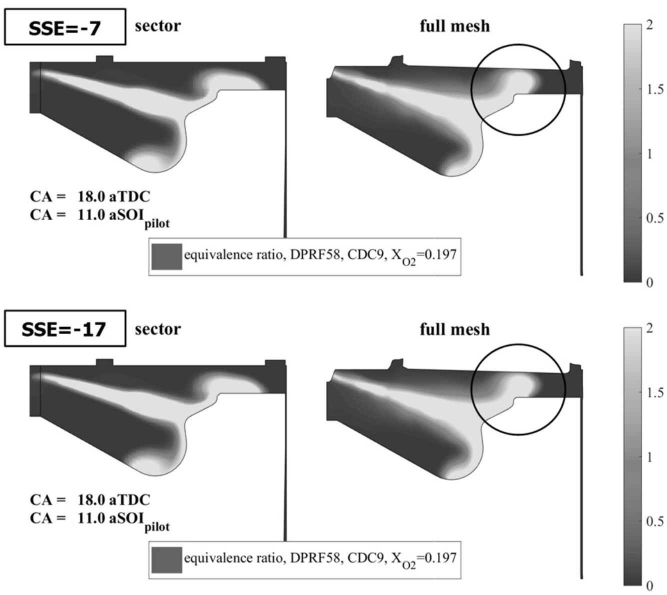

Figure 19. Formation of an upper recirculation vortex as the fuel jet hits the piston bowl: (left) sector mesh, (right) full engine mesh. Injection timing comparison: SSE = -17, -7,deg aTDC.

[30, 25]. This phenomenon was also observed using fuel-tracer PLIF in the current engine, as reported in Figure 18, where the mixture fraction on a horizontal plane bisecting the squish region is shown. Discontinuous fuel mixture regions are seen to encroach inward from the outer portions of the squish region. This cannot be explained by fuel simply traveling outward along the piston surface outward, but is justified by the creation of a recirculation zone somewhere below the observation plane. Further experimental evidence of this outer recirculation zone is provided in [32]. Accurate prediction of this phenomenon is likely to be crucial for a reliable simulation of flow and combustion inside the stepped-lip combustion chamber.

Simulation results are reported in Figure 19 for two injection timings, with pilot injections SSE = -17 and -7 deg aTDC,. Here, an effective equivalence ratio from the non-reacting environment is computed from the local fuel mole fraction by equivalence with a corresponding reactive charge, made up of air and EGR with a total oxygen mole fraction X_{O2} = 0.197 [31]. Incipient flow recirculation on the tumbling plane was captured by the full mesh approach at all injection schedules, but by none of the sector mesh simulations. Here, fuel drifted away radially, traveling along the piston surface, but no flow separation occurred. The bulk fuel jet structure was otherwise similar among the meshing approaches as far as penetration, spray cone angle, and piston targeting are concerned.

Local flow structuresNear-nozzle flow structure close to the head also had a different development: in the full mesh simulation, the fuel jet is being pulled upward, close to the head, by a lower-pressure region created by strong air entrainment close to the head (Coanda effect). The dominance of this effect may justify why varying bulk swirl ratio does not improve the sector simulation prediction, while the presence of a less coherent swirl vortex structure close to the head (full mesh) could explain the easier/faster formation of a tumbling entrainment vortex.

This was studied by looking at the Navier-Stokes momentum conservation equation, expressed along the radial coordinate of a cylindrical coordinate system.

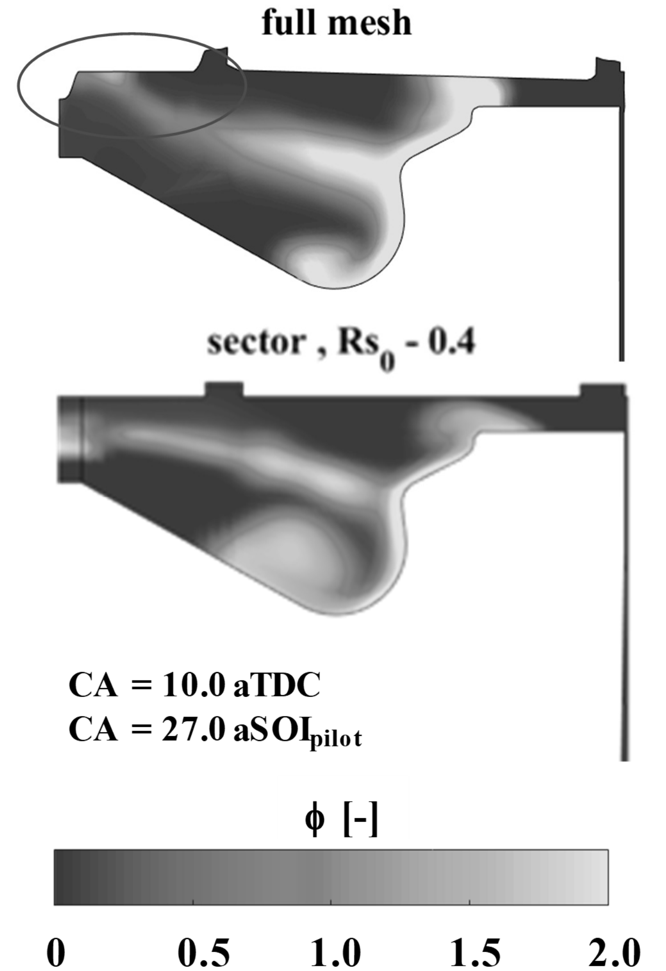

Figure 20. Predicted equivalence ration on the vertical nozzle plane using the full mesh approach or a sector mesh with reduced IVC swirl ration, $Rs_{IVC} = Rs_0 - 0.4$.

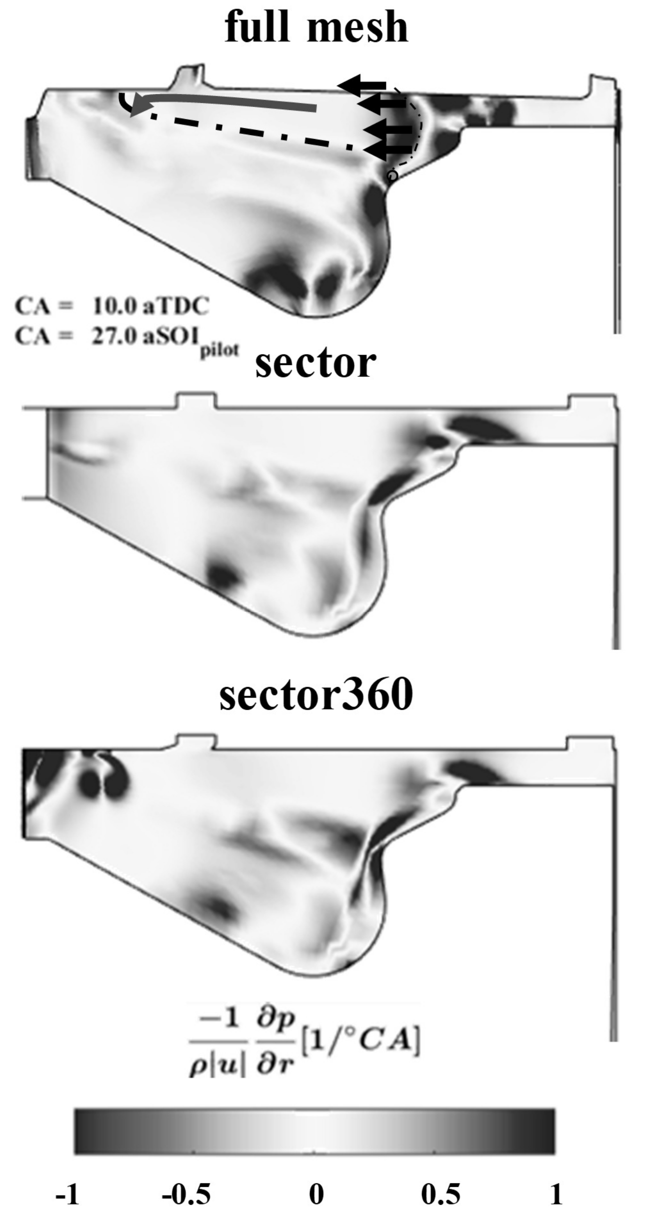

Figure 21. Normalized radial pressure gradient on the vertical nozzle plane using all mesh approaches, after the jet impact against the piston surface. Closed recirculation structure on the tumbling plane highlighted on the full mesh image.

A full description of this methodology is reported in [25]. Among the terms responsible for momentum conservation along the radial coordinate, the radial pressure gradient maps the flow separation locations (gradient changing sign), and the pressure drop contributions to achieving flow separation. As in Figure 21, with a full mesh, flow separation happened early above the piston step, and supported a self-sustained entrainment 'ring' that took the flow both inward at the step, and upward at the injector.

This suggests that the non-horizontal head shape causes it, thanks to: lower pressure regions close to the head due to the non-azimuthal valve recesses (Figure 12), fostering upward jet translation in the central region of the cylinder; and non-horizontal valve plates, causing the squish region to be slightly convergent in the two regions below the intake and the exhaust valves. In fact, in both sector simulations, no flow separation happened at the step, and there was no net pressure gradient front along the spray jet showing strong air entrainment. It should be also noted that using an appropriate-resolution body-fitted numerical mesh was likely crucial to capturing these geometry-induced flow features very close to the wall boundary layers.

Advection contributions to flow separation. Advection of radial momentum along the cylindrical coordinates (azimuthal, radial, vertical) is reported in Figure 22. Azimuthal convection only had a non-negligible role (the color scale was halved to make it more evident) in the fuel jet core. This was in line with the observation that bulk swirl ratio did not dominate the ability to generate the upper tumbling vortex. Instead, advection had a strong effect along the injection axis – a combination of radial and vertical convection. Here, noticeable differences between the full and sector360 meshes appeared. The full mesh showed much stronger advection of radial momentum mostly along the spray jet. Given similar liquid spray velocities, that supported the hypothesis of stronger air entrainment due to the formation of the upper recirculation bubble.

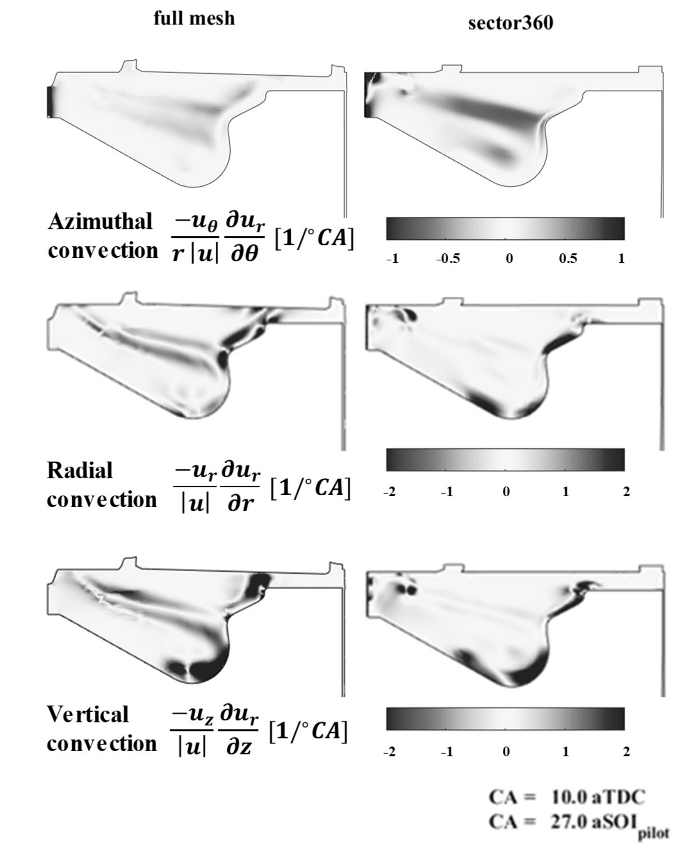

Figure 22. Advection contribution terms to the radial momentum conservation equations, with either full mesh or sector-360.

Jet to jet deviations. In the sector-360 case, jet-to-jet deviations are only due to differences in local flow field properties, as the geometry is fully symmetric. In the full mesh case, the geometry of the canted valves and their recesses above each jet depends on its azimuthal location. Figure 23 reports jet-averaged fuel vapor penetration into the combustion chamber, as the farthest location where at least 10 ppm of fuel are found, along the injection axis:

$$d_{vap} = \max_{X_{fuel} \geq 10^{-5}} \{(\mathbf{x} - \mathbf{x}_{nozzle}) \cdot \hat{\boldsymbol{n}}_{\boldsymbol{nozzle}}\}. \quad (3)$$

The jet-based standard deviation of vapor penetration (shown by the scatter bands) was small after both injection pulses, for all meshing approaches, and the difference in predicted penetration history was also small, also indicating that the set of spray models employed in this study provides reasonably grid-independent results. The location of an elbow in the vapor penetration curve, slightly after 5 deg aTDC, represented the instant when the spray jet hits the piston step and is being split between the squish and bowl regions.

Here, the additional vapor penetration comes from fuel directed into the squish, as fuel in the bowl is redirected axially backward by the bowl shape, in a U-turn. The full mesh predicted a slightly delayed timing of the fuel impact against the rim, as well as a slightly wider standard deviation of post-impact jet structure than the sector-360 predicts.

Figures 24 and 25 suggest that this greater deviation is due to the local head geometry being experienced by each jet.

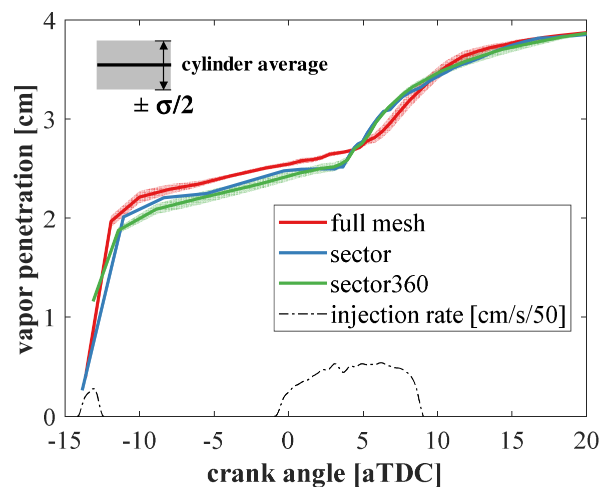

Figure 23. Vapor penetration prediction versus mesh type. Solid lines: cylinder average; shaded areas thickness: one standard deviation. Overlapped injection rate law (SSE=-17 case).

Figure 24 reports the near-TDC injection case, SSE = -17 aTDC, where the impact happens at approximately 5 deg aTDC: i.e., with high ambient density, and narrow squish height. With a sector-360 mesh, the mixture distribution of all jets is remarkably similar, while greater deviations are seen in the full mesh. The ability to form an upper recirculation bubble was predicted for all jets, even with reasonable jet-to-jet discrepancies, only with a full mesh.

Jets number 1, 3 and 6 were directed entirely below the valve faces, and experienced the most radially convergent squish volume shape; they also show the strongest flow recirculation. Jets number 4 and 5 were only almost radially directed below the valves. The strength of the recirculation zones for these jets, while well visible, is somewhat limited due to the complex geometric interaction with the valve recess. Jets number 2 and 7 experienced a fully flat head, as they crossed no valve plate regions. For them, the weakest separation structures were seen. These structures of these jets were the most similar to the structures being predicted by the sector-360 mesh.

Similar behavior was observed for the intermediate injection timing, SSE = -07 aTDC, in Figure 25. Spray impingement on the piston occurred at approximately 15 deg aTDC, and the recirculation region was already formed at 20 deg aTDC. Here, distance between the piston surface and the cylinder head at the location of impingement is larger, suggesting a weaker effect of the head geometric details onto the spray structure. However, the sector-360 mesh was still unable to predict flow separation of any of the jets. This was again seen for all jets in the full mesh, where some jet-to-jet discrepancies caused by the head geometry were still seen. In particular, for jet #2, the recirculation region was the weakest, and some degree of outward drifting along the piston surface, similar to what was predicted by the sector-360 mesh.

Mixing rate

The stoichiometric iso-surface area was used as a measure of air-fuel mixing, since these simulations were in a non-reacting environment. The stoichiometric isosurface was built from the equivalence ratio field as a level-set surface with $\phi=1.0$, employing the methodology developed in [37]. The isosurface is built as a triangulated surface whose set of nodes is found as piercing points along the mesh edges, found by linear interpolation of the nodal values in the node-centered field. The tessellation in each cell that includes the surface is then found by the marching cells algorithm.

Figure 26 shows stoichiometric iso-surface development versus meshing approach. Early mixing, represented by the initial ramp-up phase, happens at the fuel jet tip before its impact against the piston:

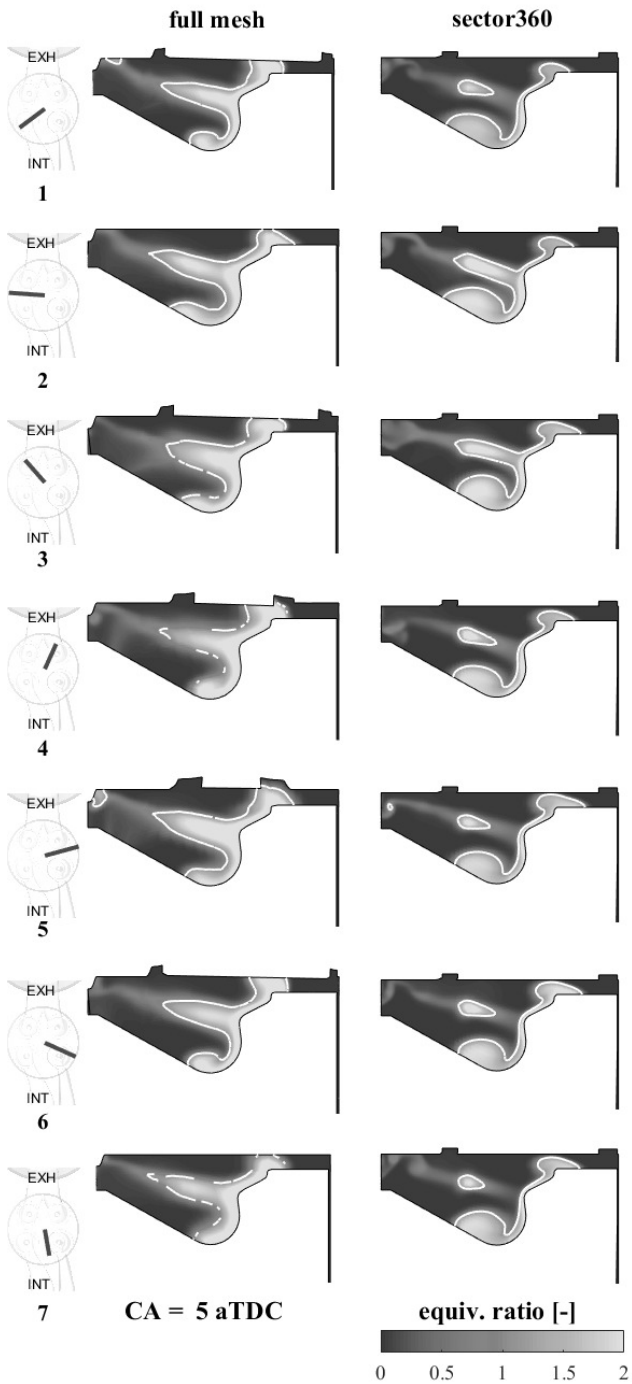

Figure 24. Jet-to-jet discrepancies in equivalence ratio predictions. SSE=-17. Left: full mesh; right: sector-360 mesh. Red lines: nozzle axis orientation as seen from the cylinder bottom.

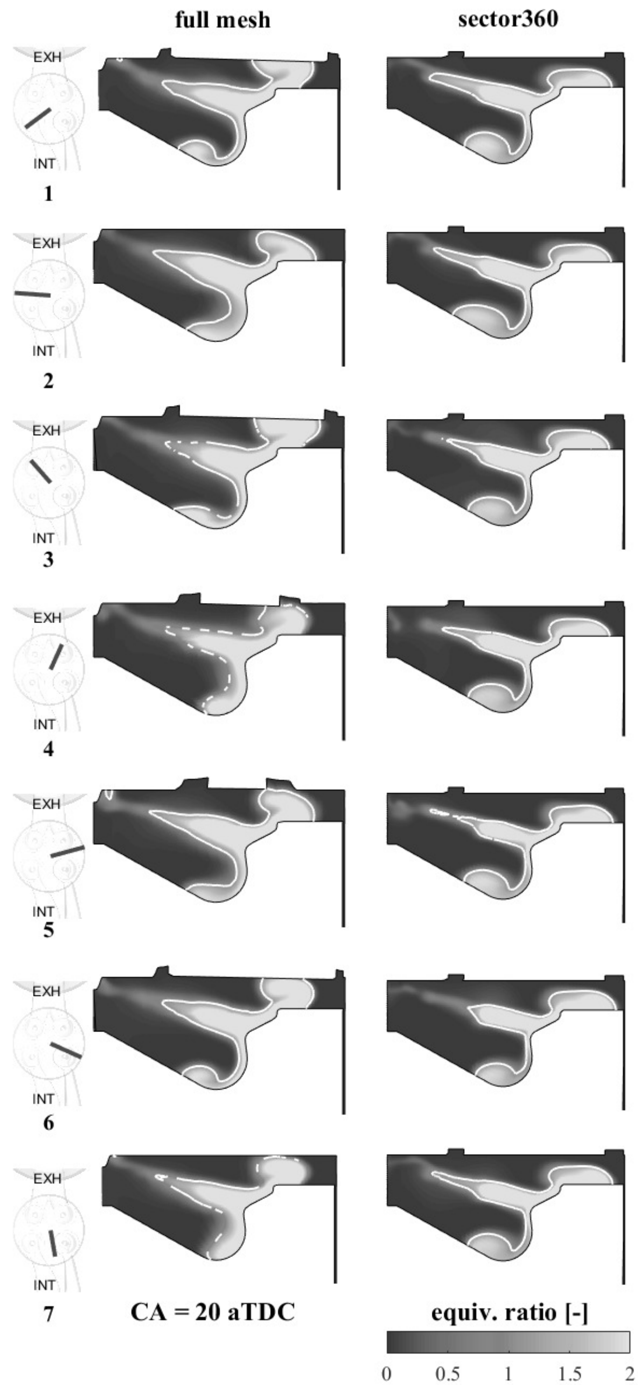

Figure 25. Jet-to-jet discrepancies in equivalence ratio predictions, after the the jet-piston impact. SSE=-07, CA=20 deg aTDC. Left: full mesh; right: sector-360 mesh. Red lines: nozzle axis orientation as seen from the cylinder bottom.

due to the large injection velocities and similar spray predictions, this behavior was insensitive to the meshing approach. Both sector-mesh approaches instead over-predicted post-impact mixing with respect to the full mesh. This suggested tangential velocity dominance, as the stoichiometric isosurface spreads out in the azimuthal direction, fostered by local swirl. Late-cycle mixing has been seen to be crucial for the global, engine-out combustion efficiency [24]. Full and sector-360 approaches showed similar behavior, suggesting that mixing predictions are are strongly affected

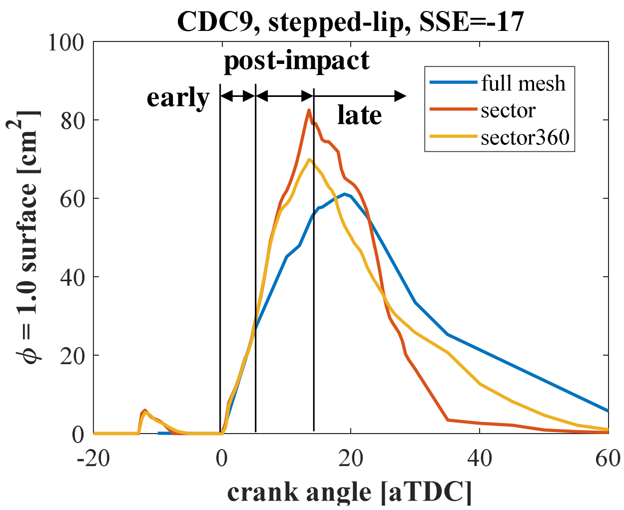

Figure 26. Stoichiometric isosurface area for the SSE = -17 case, meshing approach comparison.

by residual flow-field/turbulence non-uniformities, which are not present with the sector mesh approach. According to the sector mesh, the stoichiometric iso-surface is eliminated much more quickly than with the full mesh or sector-360 approaches.

Concluding remarks

In this study the effects of modeling engine geometric details on the accuracy of flow field and mixture formation predictions from CFD simulations of a direct-injection diesel engine were studied. Simulations of the Sandia National Laboratories optical diesel engine, equipped with a stepped-lip piston, and operating in a conventional diesel combustion mode with two injection timings, for which extensive experimental validation had been previously achieved, were used. Three modeling approaches were compared: a full-engine geometry with full-cycle simulation of intake and exhaust flows; an axisymmetric sector geometry with homogeneous field initialization at IVC; and an axisymmetric 360-degree sector geometry with direct field mapping at IVC from the full-mesh simulation. The sector mesh simplification is widely used by researchers for computational efficiency.

The following major conclusions were drawn:

- In-cylinder flow and turbulence distributions are more strongly affected by the engine's geometric details, like non-azimuthal valve recess edges, and non-horizontal valve faces slightly protruding into the combustion chamber, than by the accuracy of meshing or of the initial conditions. Non-axisymmetric details in a swirl-supported diesel engine introduce complex flow structures which modify the swirl vortex by slowing it down and by keeping it more tilted through the end of the compression stroke;

- An axisymmetric geometry cannot reproduce in-cylinder flow and turbulence quantities well throughout both compression and expansion strokes, even if the IVC swirl ratio is tuned, or if all fields at IVC are mapped from a full-geometry simulation. The swirl vortex also exhibits a different radial structure, where the tangential velocity parameter α is lower than that for a full mesh.

- Geometric details of the cylinder head in a full engine mesh cause localized azimuthal flow separation. This prevents the swirl vortex from becoming axisymmetric, through slower swirl axis precession and greater tilting angles. As a result, larger tangential velocities are seen close to the liner, and smaller velocities exist closer to the piston step. This aids early flow separation of the fuel jet above the step, and formation of a self-feeding recirculation vortex in the tumbling plane, in the region above the fuel jet. Greater turbulence production close to the walls leads to greater heat transfer, lower bulk near-TDC temperatures, and longer late-cycle mixing.

- The flow field discrepancies which descend from their approximate representations of the engine geometry preclude axisymmetric models from accurately representing the turbulent mixing enhancement mechanism of a stepped-lip piston geometry due to flow recirculation in the tumbling plane, in the upper portion of the combustion chamber, regardless of the distance between the piston surface and the cylinder head at the time of impact.

- It is important to note that resolution of subtle geometry-induced flow effects requires the use of a body-fitted mesh to obtain the necessary modeling accuracy with practical mesh sizes.

While much has been learned about the causes of the discrepancies between sector and full geometry modeling approaches in small-bore diesel engines, the impacts of other engine operating parameters (charge density, fuel rail pressure) are still not well understood. A better understanding will be needed as sector meshes are typically employed in large, design-of-experiments studies. The current work provides a fundamental, scientifically based framework within which such sensitivities can be assessed.

References

[1] P. Dimitriou, W. Wang and Z. Peng, "A piston geometry and nozzle spray angle investivation in a DI diesel engine by quantifying the air-fuel mixture," *International Journal of Spray and Combustion Dynamics,* vol. 7, no. 1, pp. 1-24, 2014.

[2] A. Vassallo, "Combustion system design and development process for modern automotive diesel engines," in *SAE 13th International Conference on Engines & Vehicle (ICE2015)*, Naples, Italy, 2015.

[3] C. Schramm, C. Gruenig, M. Brauer and M. Diezemann, "Piston Bowl Optimization for a Diesel Engine with Variable Compression Ratio," in *STAR Global Conference 2016*, Prague, 2016.

[4] M. A. Gonzalez D, G. L. Borman and R. D. Reitz, "A Study of Diesel Cold Starting using both Cycle Analysis and Multidimensional Calculations," in *SAE Technical Paper 910180*, Detroit, Michigan, 1991.

[5] A. A. Amsden, P. J. O'Rourke and T. D. Butler, "KIVA-II: A Computer Program for Chemically Reactive Flows with Sprays," Los Alamos National Laboratories LA-11560-MS, Los Alamos, NM, 1989.

[6] R. D. Reitz and C. J. Rutland, "Development and Testing of Diesel Engine CFD Models," *Progress in Energy and Combustion Science,* vol. 21, no. 2, pp. 173-196, 1995.

[7] H.-W. Ge, Y. Shi, R. D. Reitz, D. D. Wickman, G. Zhu, H. Zhang and Y. Kalish, "Heavy-Duty Diesel Combustion Optimization Using Multi-Objective Genetic Algorithm and Multi-Dimensional Modeling," in *SAE Technical Paper 2009-01-0716*, Detroit, MI, 2009.

[8] R. Shrivastava, R. P. Hessel and R. D. Reitz, "CFD Optimization of DI Diesel Engine Performance and Emissions Using Variable Intake Valve Actuation with Boost Pressure, EGR and Multiple Injections," in *SAE Technical Paper 2002-01-0959*, Detroit, MI, 2002.

[9] D. D. Wickman, P. K. Senecal and R. D. Reitz, "Diesel Engine Combustion Chamber Geometry Optimization Using Genetic Algorithms and Multi-Dimensional Spray and Combustion Modeling," in *SAE Technical Paper 2001-01-0547*, Detroit, MI, 2001.

[10] M. Bergman, J. Fredriksson and V. I. Golovitchev, "CFD-Based Optimization of a Diesel-fueled Free Piston Engine Prototype for Conventional and HCCI Combustion," *SAE International Journal of Engines,* vol. 1, no. 1, pp. 1118-1143, 2009.

[11] E. Kurtz and J. Styron, "An Assessment of Two Piston Bowl Concepts in a Medium-Duty Diesel Engine," *SAE International Journal of Engines,* vol. 5, no. 2, pp. 344-352, 2012.

[12] P. C. Miles and O. Andersson, "A review of design considerations for light-duty diesel combustion systems," *International Journal of Engine Research,* vol. 17, no. 1, pp. 6-15, 2016.

[13] F. Perini and R. D. Reitz, "FRESCO - an object-oriented, parallel platform for internal combustion engine simulations," in *28th International Multidimensional Engine Modeling User's Group Meeting at the SAE Congress*, Detroit, 2018.

[14] B.-L. Wang, P. C. Miles, R. D. Reitz and Z. Han, "Assessment of RNG Turbulence Modeling and the Development of a Generalized RNG Closure Model," in *SAE Technical Paper 2011-01-0829*, Detroit, MI, 2011.

[15] F. Perini, S. Busch, K. Zha and R. D. Reitz, "Comparison of Linear, Non-linear and Generalized RNG-based k-epsilon models for turbulent diesel engine flows," in *SAE Technical Paper 2017-01-0561*, Detroit, MI, 2017.

[16] F. Perini and R. D. Reitz, "Improved atomization, collision and sub-grid scale momentum coupling models for transient vaporizing engine sprays," *International Journal of Multiphase Flows,* vol. 79, pp. 107-123, 2016.

[17] R. D. Reitz and F. V. Bracco, "On the Dependence of Spray Angle and Other Spray Parameters on Nozzle Design and Operating Conditions," in *SAE Technical Paper 790494*, 1979.

[18] J. C. Beale and R. D. Reitz, "Modeling Spray Atomization with the Kelvin-Helmholtz/Reyleigh-Taylor Hybrid Model," *Atomization and Sprays,* vol. 19, no. 7, pp. 623-650, 1999.

[19] A. Munnannur and R. D. Reitz, "Comprehensive Collision Model for Multidimensional Engine Spray Computations," *Atomization and Sprays,* vol. 9, no. 6, pp. 597-619, 2009.

[20] D. J. Torres, P. J. O'Rourke and M. F. Trujillo, "A Discrete Multicomponent Fuel Model," *Atomization and Sprays,* vol. 13, no. 2&3, p. 42, 2003.

[21] F. Perini, A. B. Dempsey, R. D. Reitz, D. Sahoo, B. Petersen and P. C. Miles, "A Computational Investigation of the Effects of Swirl Ratio and Injection Pressure on Mixture Preparation and Wall Heat Transfer in a Light-Duty Diesel Engine," in *SAE Technical Paper 2013-01-1105*, Detroit, MI, 2013.

[22] "ECN Data Search Page," [Online]. Available: https://ecn.sandia.gov/ecn-data-search/. [Accessed 28 08 2018].

[23] S. Busch, "Light-Duty Diesel Combustion," in *DOE Vehicle Technologies Office and Hydrogen and Fuel Cells Program Annual Merit Review*, Washington, DC, 2017.

[24] S. Busch, K. Zha, E. Kurtz, A. Warey and R. C. Peterson, "Experimental and Numerical Studies of Bowl Geometry Impacts on Thermal Efficiency in a Light-Duty Diesel Engine," in *SAE Technical Paper 2018-01-0228*, 2018.

[25] S. Busch, K. Zha, F. Perini, R. D. Reitz, E. Kurtz, A. Warey and R. Peterson, "Bowl Geometry Effects on Turbulent Flow Structure in a Direct Injection Diesel Engine," in *SAE Technical Paper 2018-01-1794*, Heidelberg, Germany, 2018.

[26] S. Busch and P. C. Miles, "Parametric Study of Injection Rates With Solenoid Injectors in an Injection Quantity and Rate Measuring Device," in *ASME Paper No. ICEF2014-5583*, Columbus, Indiana, USA, 2015.

[27] "Small-Bore Diesel Engine," Sandia Mational Laboratories, 11 8 2017. [Online]. Available: https://ecn.sandia.gov/engines/engine-facilities/small-bore-diesel-engine/. [Accessed 2018].

[28] F. Perini, R. D. Reitz and P. C. Miles, "A comprehensive modeling study of in-cylinder fluid flows in a high-swirl, light-duty optical diesel engine," *Computers and Fluids,* vol. 105, pp. 113-124, 2014.

[29] F. Perini, K. Zha, S. Busch, E. Kurtz, R. C. Peterson, A. Warey and R. D. Reitz, "Piston geometry effects in a light-duty, swirl-supported diesel engine: flow structure characterization," *International Journal of Engine Research,* vol. OnlineFirst, 2017.

[30] K. Zha, S. Busch, A. Warey, R. C. Peterson and E. Kurtz, "A Study of Piston Geometry Effects on Late-Stage Combustion in a Light-Duty Optical Diesel Engine Using Combustion Image Velocimetry," in *SAE Technical Paper 2018-01-0230*, 2018.

[31] A. B. Dempsey, B.-L. Wang, R. D. Reitz, B. Petersen, D. Sahoo and P. C. Miles, "Comparison of Quantitative In-Cylinder Equivalence Ratio Measurements with CFD Predictions for a Light Duty Low Temperature Combustion Diesel Engine," *SAE Int. J. Engines,* vol. 5, no. 2, pp. 162-184, 2012.

[32] B. R. Petersen and P. C. Miles, "PIV Measurements in the Swirl-Plane of a Motored," *SAE Int. J. Engines,* vol. 4, no. 1, pp. 1623-1641, 2011.

[33] F. Perini, K. Zha, S. Busch, P. C. Miles and R. D. Reitz, "Principal Component Analysis and Study of Port-Induced Swirl Structures in a Light-Duty Optical Diesel Engine," in *SAE Technical Paper 2015-01-1696*, Detroit, MI, 2015.

[34] K. Zha, S. Busch, P. C. Miles, S. Wijeyakulasuriya, S. Mitra and K. Senecal, "Characterization of Flow Asymmetry During the Compression Stroke Using Swirl-Plane PIV in a Light-Duty Optical Diesel Engine with the Re-entrant Piston Bowl Geometry," *SAE International Journal of Engines,* vol. 8, no. 4, pp. 1837-1855, 2015.

[35] F. Perini, D. Sahoo, P. C. Miles and R. D. Reitz, "Modeling the Ignitability of a Pilot Injection for a Diesel Primary Reference Fuel: Impact of Injection Pressure, Ambient Temperature and Fuel Mass," *SAE Int. J. Fuels Lubr.,* vol. 7, pp. 48-64, 2014.

[36] Z. Han and R. D. Reitz, "A temperature wall function formulation for variable-density turbulent flows with application to engine convective heat transfer modeling," *International Journal of Heat and Mass Transfer,* vol. 40, no. 3, pp. 613-625, 1997.

[37] F. Perini, K. Hiraoka, K. Nomura, A. Yuuki, Y. Oda, C. J. Rutland and R. D. Reitz, "An Efficient Level-Set Flame Propagation Model for Hybrid Unstructured Grids using the G-Equation," *SAE International Journal of Engines,* vol. 9, no. 3, pp. 1409-1424, 2016.

Contact Information

Federico Perini
perini@wisc.edu

Acknowledgments

This work was performed under Sandia Subcontract 1890589, 1, sponsored by the United States Department of Energy, Office of Vehicle Technologies, with program managers Gupreet Singh and Michael Weismiller.

Sandia National Laboratories is a multi-mission laboratory managed and operated by National Technology and Engineering Solutions of Sandia, LLC., a wholly owned subsidiary of Honeywell International, Inc., for the U.S. Department of Energy's National Nuclear Security Administration under contract DE-NA-0003525. The views expressed in the article do not necessarily represent the views of the U.S. Department of Energy or the United States Government.

Appendix A: A Conservative Field Mapping scheme

A conservative scheme for finite volume, mesh-based data was established in order to map field quantities from the full engine geometry to the sector-360 mesh. It is required that both donor field data and the receiver mesh come with a suitable topology; accepted cell types are tetrahedra, pyramids, wedges (triangular prisms), or hexahedra, as reported in Figure 27.

Field interpolation strategy.

Field interpolation from the donor mesh is node-based for both node- and cell-centered fields. An isoparametric equivalent of each cell is employed to perform multilinear interpolation inside the domain. The interpolation location in the receiver mesh is either its nodes, for a node-centered field, or its cell centroids, for a cell-centered field.

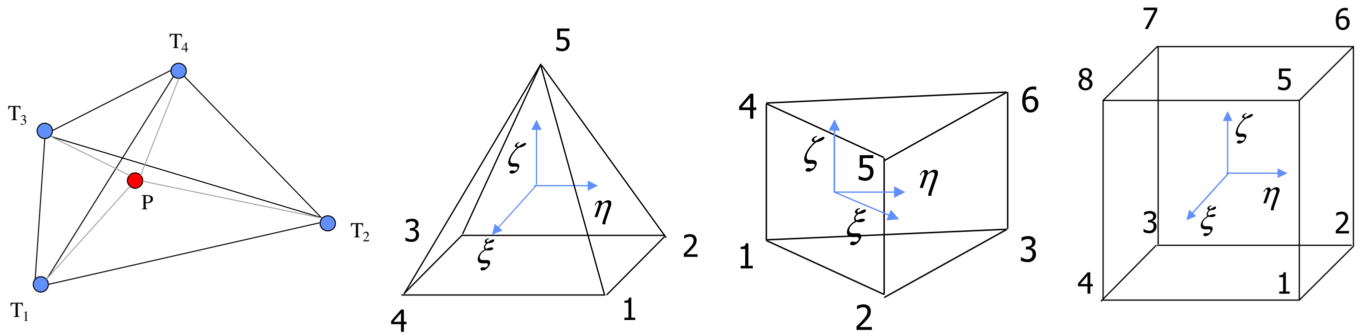

Figure 27. Accepted cell types for the field remapping scheme, and their natural coordinate systems. Left to right: tetrahedron, pyramid, wedge (triangular prism), hexahedron.

<u>Tetrahedron</u>. For a tetrahedron, four barycentric coordinates are employed to map the local position of any interior points:

$$\mathbf{P} = [x \quad y \quad z] \rightarrow [\chi_1 \quad \chi_2 \quad \chi_3 \quad \chi_4]$$

An interior point P splits the tetrahedron into four smaller tetrahedra, each of them drawn by the point with an opposite triangular face. Their volumes are:

$$\begin{aligned} V_1 &= V(PT_2T_3T_4) \\ V_2 &= V(PT_1T_3T_4) \\ V_3 &= V(PT_1T_2T_4) \\ V_4 &= V(PT_1T_2T_3) \end{aligned}$$

Each barycentric coordinate $\chi_i \in [0,1]$ represents a linear weight, corresponding to the ratio between the volume of each smaller tetrahedron with the bulk cell volume:

$$\chi_i = V_i / V$$

Barycentric coordinates are found as follows:

$$\begin{aligned} \chi_1 &= +sign\Big((\mathbf{T}_1 - \mathbf{T}_4) \cdot \big((\mathbf{T}_2 - \mathbf{T}_4) \times (\mathbf{T}_3 - \mathbf{T}_4)\big)\Big) \cdot \big[(\mathbf{P} - \mathbf{T}_4) \cdot \big((\mathbf{T}_2 - \mathbf{T}_4) \times (\mathbf{T}_3 - \mathbf{T}_4)\big)\big] \\ \chi_2 &= +sign\Big((\mathbf{T}_1 - \mathbf{T}_4) \cdot \big((\mathbf{T}_2 - \mathbf{T}_4) \times (\mathbf{T}_3 - \mathbf{T}_4)\big)\Big) \cdot \big[(\mathbf{T}_3 - \mathbf{T}_4) \cdot \big((\mathbf{T}_1 - \mathbf{T}_4) \times (\mathbf{P} - \mathbf{T}_4)\big)\big] \\ \chi_3 &= -sign\Big((\mathbf{T}_1 - \mathbf{T}_4) \cdot \big((\mathbf{T}_2 - \mathbf{T}_4) \times (\mathbf{T}_3 - \mathbf{T}_4)\big)\Big) \cdot \big[(\mathbf{T}_2 - \mathbf{T}_4) \cdot \big((\mathbf{T}_1 - \mathbf{T}_4) \times (\mathbf{P} - \mathbf{T}_4)\big)\big] \\ \chi_4 &= +sign\Big((\mathbf{T}_1 - \mathbf{T}_4) \cdot \big((\mathbf{T}_2 - \mathbf{T}_4) \times (\mathbf{T}_3 - \mathbf{T}_4)\big)\Big) \cdot \big[(\mathbf{T}_1 - \mathbf{P}) \cdot \big((\mathbf{T}_2 - \mathbf{P}) \times (\mathbf{T}_3 - \mathbf{P})\big)\big] \end{aligned}$$

The interpolated value for any field ϕ follows weight interpolation with the barycentric weights:

$$\phi(\mathbf{P}) = \sum_{i=1}^{4} \chi_i \phi(\mathbf{T}_i)$$

<u>Hexahedron</u>. Trilinear interpolation based on natural coordinates is employed for hexahedral cells:

$$\mathbf{P} = [x \quad y \quad z] \rightarrow \boldsymbol{\xi} = [\xi \quad \eta \quad \zeta] \in [-1,1]$$

Natural coordinates employ a local, normalized coordinate system centered at the cell's centroid. Eight nodal weights define the trilinear field interpolation procedure are expressed as:

$$N_i = \frac{1}{8}(1+\xi\xi_i)(1+\eta\eta_i)(1+\zeta\zeta_i), \quad i = 1,\cdots,8$$

and represent the mapping between the Cartesian and the local coordinate systems:

$$\mathbf{J} = \frac{\partial x_j}{\partial \xi_i} = \begin{bmatrix} \frac{\partial x}{\partial \xi} & \frac{\partial y}{\partial \xi} & \frac{\partial z}{\partial \xi} \\ \frac{\partial x}{\partial \eta} & \frac{\partial y}{\partial \eta} & \frac{\partial z}{\partial \eta} \\ \frac{\partial x}{\partial \zeta} & \frac{\partial y}{\partial \zeta} & \frac{\partial z}{\partial \zeta} \end{bmatrix} = \begin{bmatrix} \frac{\partial N_1}{\partial \xi} & \cdots & \frac{\partial N_8}{\partial \xi} \\ \vdots & \ddots & \vdots \\ \frac{\partial N_1}{\partial \zeta} & \cdots & \frac{\partial N_8}{\partial \zeta} \end{bmatrix} \cdot \begin{bmatrix} x_1 & y_1 & z_1 \\ \vdots & \vdots & \vdots \\ x_8 & y_8 & z_8 \end{bmatrix}$$

Because the weight functions have non-linear dependency on the local coordinates, an iterative procedure has to be established, as follows:

1. Compute Cartesian centroid: $\mathbf{C} = \frac{1}{8}\sum_{i=1}^{8}\mathbf{x}_i$
2. Compute Hexahedron Jacobian matrix: $\mathbf{J} = \begin{bmatrix} 1 & -1 & -1 & 1 & 1 & -1 & -1 & 1 \\ 1 & 1 & -1 & -1 & 1 & 1 & -1 & -1 \\ -1 & -1 & -1 & -1 & 1 & 1 & 1 & 1 \end{bmatrix} \cdot \begin{bmatrix} x_1 & y_1 & z_1 \\ \vdots & \vdots & \vdots \\ x_8 & y_8 & z_8 \end{bmatrix}$
3. Invert Jacobian matrix: $\mathbf{J^{-1}} = inv3x3(\mathbf{J})$
4. Establish Newton-Raphson procedure
    a. Initialize iterate as cell centroid $\mathbf{X_0} = \mathbf{C}$
    b. Initialize solution with first-order derivative at the centroid: $\boldsymbol{\xi}_\mathbf{0} = (\mathbf{J}^{-1})^T \cdot (\mathbf{P} - \boldsymbol{X}_\mathbf{0})$
    c. Update iterate $\boldsymbol{\xi}_\mathbf{k+1} = \boldsymbol{\xi}_k + (\mathbf{J}^{-1})^T \cdot (\mathbf{P} - \mathbf{X}_{\boldsymbol{k}})$
    d. Update shape functions $N_i = N_i(\boldsymbol{\xi}_{k+1})$
    e. Update iterate in Cartesian coordinates $X_{k+1} = \sum_{i=1}^{8} N_i\mathbf{x}_i$
    f. Check for convergence $\|\mathbf{P} - \boldsymbol{X}_{\boldsymbol{k}}\| < \varepsilon$

Convergence to ε = 1e-4 is usually achieved in less than 3-4 iterations. Based on the local coordinates, one has the corresponding weighting functions and can perform trilinear interpolation as:

$$\phi(\mathbf{P}) = \sum_{i=1}^{8} N_i\big(\boldsymbol{\xi}(\boldsymbol{P})\big)\,\phi(\boldsymbol{x}_i)$$

Pyramid. Pyramidal elements are treated as 5-node, degenerate hexahedra, where the top face is collapsed onto the apex point. According to the local coordinate center definition of Figure 27, The nodal weight functions become:

$$N_i = \begin{cases} \frac{1}{8}(1+\xi\xi_i)(1+\eta\eta_i)(1+\zeta\zeta_i), & i = 1,2,3,4 \\ \frac{1}{2}(1+\zeta), & i = 5 \end{cases}$$

Wedge (triangular prism). Similarly, wedge elements are treated as degenerate hexahedra, with a right face collapsed onto an edge. Using this assumption, the local nodal weight functions become:

$$N_i = \begin{cases} \frac{1}{8}(1+\xi\xi_i)(1+\eta\eta_i)(1+\zeta\zeta_i), & i = 1,2,4,5 \\ \frac{1}{4}(1+\eta)(1-\zeta), & i = 3 \\ \frac{1}{4}(1+\eta)(1+\zeta), & i = 6 \end{cases}$$

Wall boundary interpolation.

Cells neighboring a wall boundary are usually meshed such that appropriate resolution normal to the wall is achieved, as requested for turbulence modelling. Hence, gradients in the wall-normal direction are typically stronger than tangent to the wall surface. 3D multilinear interpolation such as done for the interior can introduce non-negligible errors in cases where non-planar surfaces are represented by cells whose height normal to the walls is thin. In case of a cylinder liner, different mesh resolutions could also lead to nodes in the new mesh falling outside of the donor mesh domain (as illustrated in Figure 28).

Figure 28. Near wall interpolation: (left) mesh nodes on a cylindrical surface, seen from above, can fall outside a previous mesh of the same surface. (right) schematic of wall face interpolation.

Near-wall interpolation was hence implemented as a 2D surface interpolation problem (for triangle or quad faces). A nearest-neighbor, kd-tree based search structure is built and available for fast search within the donor mesh wall topology. The interpolation point is first projected onto its nearest wall face plane. Then, 2D bilinear interpolation is performed using nodal data of the wall face only. For nodes falling outside the donor mesh, the same procedure is applied.